UNIVERSITÀ DEGLI STUDI DI PADOVA

Dipartimento di Fisica e Astronomia "Galileo Galilei"

Master Degree in Physics

Final Dissertation

Infrared Dispersion Interferometer for Plasma Diagnostics

Thesis supervisor

Prof. Leonardo Giudicotti

Thesis co-supervisor

Dr. Donatella Fiorucci

Candidate

Miriam La Matina

Academic Year 2021/2022

Table of Contents

Abstract

In the frame of the diagnostic development for the Divertor Tokamak Test facility (DTT), a new Italian tokamak device dedicated to investigating alternative power exhaust solutions for the nuclear fusion DEMOnstration Power Station (DEMO), a study on a dispersion interferometer has been proposed, with the intention of taking advantage of the benefits of this technique in the electron density measurements.
The time evolution of electron density in magnetically confined plasmas is commonly measured using interferometry: in particular, in fusion experiments interferometer instruments are implemented to sense changes in the index of refraction of the plasma that is related to the electron density, allowing high time resolution and low measurement error.
The vibration-induced phase shift that is unavoidable in the measurement determines the need for compensation, to separate the contribution to the phase shift due to the plasma electron density. A new technique suitable for compensating vibration effects is dispersion interferometry.
In the dispersion interferometer two beams with different wavelengths are used, one derived from the other by second-harmonic generation.
In this work, two different designs of this instrument are studied: the homodyne scheme and the heterodyne one.
The simplest version is the homodyne scheme, in which the two beams that interfere fall on the same detector. This instrument has been designed and built, changing different configurations to overcome some obstacles until the final setup has been defined.
Some interferometric test measurements have been recorded, and the sensitivity of this instrument has been evaluated.
The heterodyne scheme of the instrument has been studied and designed.
In a heterodyne scheme, an Acousto Optic modulator (AOM) is included in the optical path of one of the two beams.
Some tests on the modulating system implemented have been carried out.
A theoretical study on some solutions to separate the paths of the beams in the heterodyne configuration has been done, introducing a deflection of the beams with one or two prisms. This represents an innovative solution, which guarantees a better superposition of the beams, which will share all the optical elements, eliminating the vibrational components of the phase difference.
During this work, it was also visited the experiment PROTO-SPHERA, at the laboratories of ENEA, Frascati, where a homodyne interferometer is operating on the machine.
The system was modified and realigned. Some data from the experiment have also been analyzed, to estimate the electron density of the plasma produced inside the machine.

Introduction

1.1 Interferometric diagnostics in Fusion Plasmas

In modern fusion plasma machines, several diagnostics are used, to achieve the largest amount of information about the properties of the plasma generated. These diagnostics exploit different physical properties, interacting with the plasma itself or as passive measures.
Among the non-perturbing methods of diagnostics, some of the most accurate use an electromagnetic (EM) wave as a probe inside the plasma. With the hypothesis of not too great intensity, so that the perturbation it creates is negligible, the wave propagates in the plasma, interacting with it.
The system is studied under some assumptions: the EM wave is considered plane, monochromatic and polarized; the ions are supposed not to be affected by the wave (due to their large masses); the motion of the electrons is due only to the interaction with the wave; collisions are neglected.
The complex interaction can be described by studying the refractive index equation for the plasma. Because of the magnetic field, the electrical properties of the plasma are highly anisotropic.
The basic equation describing the refractive index for interferometry is the *Appleton-Hartree* dispersion equation[1]. It gives the refractive index $N = \frac{k}{k_0} = \frac{kc}{\omega}$ for an electro-magnetic wave that propagates through a magnetized plasma under the assumptions expressed before.
The equation is:

$$N^2 = 1 - \frac{X[1-X]}{1 - X - \frac{1}{2}Y^2 sin^2\theta \pm \sqrt{(\frac{1}{2}Y^2 sin^2\theta)^2 + [1-X]^2 Y^2 con^2\theta}} \tag{1.1}$$

where $X = (\omega_p/\omega)^2$, $Y = \omega_{ce}/\omega$, with $\omega_p = \sqrt{\frac{n_e e^2}{m_e \varepsilon_0}}$ the plasma frequency and $\omega_{ce} = \frac{eB}{m_e}$ the electron cyclotron frequency. Also, ω is the frequency of the EM wave, and θ the angle between the wave vector and the magnetic field.
Eq. 1.1 has two solutions, which will depend on the polarization of the wave considered. Some special cases are now treated, obtaining the solutions for this equation.
The solution for the refractive index corresponding to the case of a wave polarized such to have its electric field E parallel to the magnetic field B, also defined *ordinary wave*, is:

$$N_o = \sqrt{1 - \frac{\omega_p^2}{\omega^2}} \tag{1.2}$$

If instead the wave has an electric field normal to the magnetic field and is thus defined as *extraordinary wave*, the refractive index solution is:

$$N_e = \sqrt{1 - \frac{\omega_p^2}{\omega^2} \frac{\omega^2 - \omega_p^2}{\omega^2 - \omega_p^2 - \omega_{ce}^2}} \tag{1.3}$$

where $\omega_{ce} = \frac{eB}{m_e}$ is the electron cyclotron frequency.
When, otherwise, the wave is circularly polarized (left or right) and propagates along the magnetic field direction, then the two solutions for the refractive index are:

$$N_{\pm} = \sqrt{1 - \frac{\omega_p^2}{\omega^2}\frac{\omega}{\omega \pm \omega_{ce}}} \tag{1.4}$$

The index of refraction of a medium is measurable by using electromagnetic waves for which the medium is transparent: in the case of high-density plasmas, they are transparent as long as the plasma frequency ω_p is smaller than the frequency of the probing wave, ω[2].
Interferometry is the principal experimental technique that allows measuring of the refractive index of the plasma. So, for interferometry the condition $\omega \gg \omega_p$ is chosen, a condition which implies that the equation describing the refractive index is:

$$N \simeq \sqrt{1 - \frac{\omega_p^2}{\omega^2}} \tag{1.5}$$

which is the refractive index of the ordinary wave.
This relation is applicable for all the different cases of polarization and orientation of the B field. Defining the critical density by the condition $\omega = \omega_p$, which corresponds to the value of density above which the beam is reflected back by the plasma, it is possible to see that the condition imposed on ω ($\omega \gg \omega_p$) corresponds to $n_e \ll n_c$, where $n_c = \frac{m_e \varepsilon_0}{e^2}\omega^2$.
The refractive index, thus, can be rewritten as $N = \sqrt{1 - \frac{n_e}{n_c}} \simeq 1 - \frac{1}{2}\frac{n_e}{n_c}$.
The phase accumulated by the EM wave traveling inside the plasma for a distance L is

$$\phi = \int_L k dl = \int_L \frac{N\omega}{c} dl \tag{1.6}$$

If now we consider the case where the same wave propagates along two paths of the same length L, one in vacuum and one in the plasma, the phase difference between these two waves is

$$\Delta\phi = \int_L (k - k_0) dl = \int_L (N-1)\frac{\omega}{c} dl = \frac{\omega}{2cn_c}\int_L n_e dl \tag{1.7}$$

The phase change of the transmitted wave gives a measure of the line integral of the electron density inside the plasma, which will be called *line electron density*.
To obtain a good knowledge of the density distribution, the plasma needs to be probed along different chords. The line density integral relation must be inverted to obtain an estimate of the density: various methods could be implemented, such as Abel inversion in the simplest case, or function parameterization.

The total phase shift measurable with an interferometric system is, however, composed of other terms beyond the one related to the refractive index of the plasma. If the two waves have different geometric paths (geometric path difference Δ), there will be a constant phase due to this difference: $\phi_{geom} = \frac{2\pi\delta}{\lambda}$.
Furthermore, if the optical system is exposed to vibrations, there will be an additional phase change related to that: $\phi_{vib}(t) = \frac{2\pi\delta(t)}{\lambda}$, where $\delta(t)$ is the displacement related to the vibrations.
The total phase of a wave passing through the plasma is

$$\phi_{tot} = \phi_{pl}(t) + \phi_{vib}(t) + \phi_{geom} \tag{1.8}$$

To limit as much as possible the constant phase related to the geometric path, one can choose two waves with paths as similar as possible.

For the vibrational components, it is not possible to eliminate them from the experimental setup. In general it can be reduced, but not eliminated: interferometers are usually mounted on vibration isolated optical benches, typically shaped as a "C" frame around the plasma.
A methodology applied to compensate for vibrations is *two-color interferometry.* This technique is characterized by two different laser sources: the phase is measured using both beams, and from these values the contribution of vibrations on the measurement is eliminated.
However, it requires two laser sources and implies many problems related to the alignment of the beams and the difference in their optical path.
A new technique suitable for compensating vibration effects is the *dispersion interferometer.* In the dispersion interferometer two beams with different wavelengths are used, one derived from the other by second-harmonic generation.

1.2 Second Harmonic Generation (SHG)

In classical linear optics, the relation between the polarization of a medium $\overrightarrow{P}$ and the applied electric field $\overrightarrow{E}$ is described by a linear equation:

$$\overrightarrow{P} = \varepsilon_0 \; \chi \; \overrightarrow{E} \tag{1.9}$$

where χ is the dielectric susceptibility.
Working with lasers, the electric fields involved are very high, thus the linear relation just explained is not a good approximation, since $\overrightarrow{P}$ is related to higher-order powers of the electric field. The non-linearity of the response may cause an energy exchange between waves at different frequencies.
In our case, the focus is on second-harmonic generation (SHG), which is a nonlinear optical process where, employing the interaction with a material characterized by second-order nonlinear susceptibility, a laser beam at frequency ω is partially converted to a coherent beam with frequency 2ω.

To explain the physical phenomenon, the induced non-linear polarization, which will be named P_{n-l}, is related to E by the following equation:

$$P_{n-l} = 2 \; d \; \varepsilon_0 E^2 \tag{1.10}$$

with d a coefficient.
The physical origin of this relation derives from the non-linear deformation of the outer electrons of the atoms of the lattice, due to the high electric field to which they are subjected[3].
The second-order term becomes comparable to the linear one for an electric field $E \simeq \chi/d$. Since $\chi \simeq 1$, the strength of the field, for which the non-linear term becomes relevant, is represented by $1/d$. This term is expected to be of the same order as the electric field.

Considering a monochromatic plane wave of frequency ω, propagating along the z-direction, through a non-linear crystal, it is possible to write the electric field of this wave as

$$E_\omega = \frac{1}{2} \left[E(z, \omega) exp(i(\omega t - k_\omega z)) + c.c. \right] \tag{1.11}$$

with *c.c.* the complex conjugate of the other term, and $k_\omega = \frac{n_\omega \omega}{c}$, n_ω the refractive index for frequency ω.
Substituting this equation for the electric field in Eq. 1.10, it is possible to find an equation for the non-linear polarization:

$$P_{n-l} = \frac{\varepsilon_0 \; d}{2} \left[E^2(z, \omega) exp(i(2\omega t - 2k_\omega z)) + c.c. \right] \tag{1.12}$$

The polarization wave oscillates at frequency 2ω and has a propagating constant $k_{2\omega}$. This corresponds to the generation of a wave of double frequency with respect to the former one: this phenomenon is thus called Second Harmonic generation.
The radiated SH electric field can be written

$$E_{2\omega} = \frac{1}{2}\left[E(z, 2\omega)exp(i(2\omega t - k_{2\omega} z)) + c.c.\right] \tag{1.13}$$

with $k_{2\omega} = \frac{2\ n_{2\omega}\omega}{c}$.

A comparison between Eq. 1.12 and 1.13 shows that the condition which must be satisfied for this process to be successful is:

$$k_{2\omega} = 2k_{\omega} \tag{1.14}$$

If this relation for the phase is not fulfilled, the SH wave does not grow cumulatively with the distance. Eq. 1.14 is called *phase-matching* condition.

The phase-matching condition can be satisfied with an anisotropic crystal. Given the direction of propagation, and given the birefringence of the medium, the wave can be described as two different linearly polarized waves, with different phase velocities, related to the different refractive index for the polarization directions.

One of the directions is perpendicular to the optical axis of the crystal, and the wave alongside this direction is called *ordinary wave*. Its refractive index n_o is independent of the direction of propagation. The wave in the other direction of polarization is called *extraordinary wave*. Its refractive index $n_e(\theta)$ depends on the angle θ with respect to the optic axis (Fig.1.1) and can have different values in the range between n_o and n_e, corresponding to the extraordinary index, when the direction of propagation is perpendicular to the optical axis[3].
The phase-matching condition (Eq. 1.14) can be translated into

$$n_e(2\omega, \theta_m) = n_o(\omega) \tag{1.15}$$

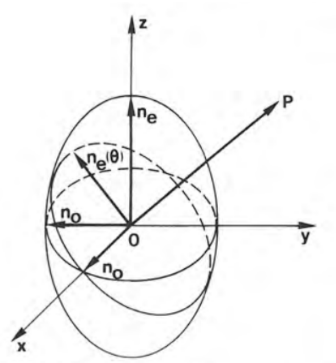

Figure 1.1: Scheme of the index ellipsoid for a positive uniaxial crystal[3].

The phase-matching conditions is obtained equaling the two refractive indices, the ordinary one and the extraordinary one, each for one of the wavelengths. The feasibility of this condition is made possible by the dependence of the extraordinary wave from the angle θ and the condition is fulfilled for a specific range of angles around a certain value θ_m.
To work in such a condition is thus necessary to carefully align the beam with the crystal so that the angle between the direction of propagation of the beam and the axis of the crystal is within the range of the phase-matching angle.

There are several schemes for choosing the polarization of the wave with respect to the crystal axis. Based on the choice of the polarization associated with the incoming wave, the crystal may be associated with different types: in the case of the crystal used during this study, the signal, which is the input beam, has ordinary polarization, and the idler, which is the second-harmonic generated beam has extraordinary polarization. This particular case is called ”type-I phase matching”.
In particular, the phase-matching condition used in this work is critical, in the sense that the technique is sensitive to misalignment of the beam since only a finite (and small) range of beam

angles give the phase-matching (this range is called phase-matching bandwidth).
In critical phase-matching, there is also a temperature dependence on the phase-matching angle ϕ[4].

The conversion of the incoming wave into SH wave is characterized by a certain conversion coefficient. Given the limited dimension of the crystal, only a fraction of the incident power can be transformed into the SH wave.
The normalized conversion efficiency for SHG in bulk crystals is defined by the following equation[5]:

$$\eta_{nor,SHG,Bulk} = \frac{2\,\omega_1^3\,d_{eff}^2\,\hbar(0,\xi)}{\pi\,n_1\,n_3\,\epsilon_0\,c^4} \quad , \tag{1.16}$$

where ω_1 is the angular frequency for the fundamental beam, d_{eff} is the effective nonlinear optical coefficient of the crystal, $\hbar(0,\xi)$ is the Boyd-Kleinman parameter[6] which describes how tightly the beam is focused into the crystal, n_1 is the index of refraction of the crystal at the fundamental wavelength, n_3 is the index of refraction of the crystal at the second-harmonic wavelength, ϵ_0 is the permittivity of free space, and c is the speed of light[5]. The output second-harmonic power at the exit of the crystal is given by the equation[5]:

$$P_{sh} = \eta_{nor,SHG,Bulk} P_f^2 L \quad , \tag{1.17}$$

where P_f is the fundamental power inside the crystal and L is the crystal length (10 mm).
the crystal used during this work is a Lithium triborate (LBO) crystal of dimensions $10 \times 3 \times 3$ mm. The characteristics of the system studied are: $L = 10$ mm, $\omega_1 \simeq 1.2\ 10^{15}$, $n_1 \simeq n_3 \simeq 1.6$, $d_{eff} \simeq 9.7\ 10^{-13}$ and $\hbar(0,\xi) \simeq 1$ (that represent a good approximation given the values of the numerical aperture and the typical values of the Rayleigh length considered) and the input power used is equal to 220 mW. For these conditions, the expected second harmonic power is $P_{sh} \simeq 0.9$ μW.

1.3 Dispersion Interferometer

In the early 1980s, the dispersion interferometer (DI) was introduced[7],[8]: it is a special common-path two-color interferometer based on a single laser source, the second color being the second harmonic of the fundamental radiation, produced with second harmonic generation (SHG).
Given that the second beam is generated from the fundamental one, some configuration can be achieved with a common path for the two beams. This scheme assures electron density measurements that are less sensitive to vibrations.
This kind of interferometer has been implemented in various plasma machines[9] , [10], and the results are very promising. The DI can achieve excellent accuracy and sensitivity. Moreover, this type of instrument assures impressive stability, reducing the realignment time requirement. The DI is also intrinsically calibrated since it directly measures the absolute phase shift acquired by the two beams when traveling through the plasma.[10].
The implementation of a simple homodyne dispersion interferometer (which will be described in Par. 3.1), with a continuous-wave (cw) laser, to improve time resolution too, requires only a few simple and commercially available optical components, nonlinear crystals, detectors, and minimal data processing, giving an excellent performance.

In the study [9] a comparison with a two-color interferometer equipped with a CO2 laser, with $\lambda = 10.6$ μm, and compensation at 0.63 μm wavelength, shows that the DI system possesses sensitivity and temporal resolution ten times higher for the same wavelength[9]. The DI has been

tested on a gas-dynamic trap, and its performance makes it possible to consider the applicability of such a measuring scheme to contemporary large tokamaks[9], [10].
Under the typical conditions of large plasma experiments (high level of vibrations, substantial plasma density gradients and strong magnetic field, and high levels of neutron and gamma radiation) the use of DI can be preferable, as compared to traditional schemes.

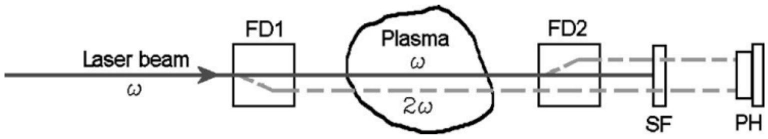

Figure 1.2: Principal scheme of the Dispersion Interferometer (DI), where the first crystal is defined as FD1, and the second one as FD2, since they work as frequency doublers. The SF is a selective filter that only let the second harmonic (2ω) pass; the PH is the photo detector that collects the output signal. The fundamental (F, with frequency ω) beam is described by the solid line, while the second harmonic (SH, with frequency 2ω) beam is described by the dashed line.[11]

A brief description of the typical layout is now explained. The basic scheme of the system is shown in Fig. 1.2.
The input beam is generated by a laser. Then the beam passes through a nonlinear crystal, in order to generate the Second Harmonic (SH) beam.
Both of the beams pass through the plasma and interact with it, acquiring a phase difference due to the refractive index of the plasma, as explained in Par. 1.1. This phase difference contains information about the electron density value.
The fundamental beam, then, passes through a second nonlinear crystal, identical to the one introduced before, which produces a second SH beam. In the end, it is possible to collect the interference between the two SH beams, and from that derive an estimate of the line electron density. The measure is not affected by vibrations.

With an analysis similar to the one carried out for the general interferometric instrument in Par. 1.1, it is possible to obtain a relation between the phase difference between the two SH beams:

$$\begin{aligned}\Delta\phi = 2\phi_F(\omega) - \phi_{SH}(2\omega) = \frac{2\omega}{c}\int [n_F(\omega) - n_{SH}(2\omega)]\ dl \simeq \\ \simeq \frac{2\omega}{c}\int \left[\left(-\frac{1}{2}\frac{n_e}{n_c(\omega)}\right) - \left(-\frac{1}{2}\frac{n_e}{n_c(2\omega)}\right)\right] dl = -\frac{\omega}{2cn_c(\omega)}\frac{3}{2}\int n_e\ dl = -\frac{3}{2}K\lambda \int n_e\ dl\end{aligned} \tag{1.18}$$

where $\phi_F(\omega)$ is the phase acquired by the F beam passing through the plasma, $\phi_{SH}(2\omega)$ is the phase acquired by the SH beam passing through the plasma, $n_c(\omega)$ is the critical density corresponding to a wave with frequency ω, and K a constant such that $\frac{3}{2}\ K = 4.2210^{-15}\ m$.
This is the simplest description of the system. During this work different configurations have been designed and analysed, each with some differences from this basic description. We will go into detail in the next paragraphs.

1.4 DTT Experiment

During this work, the dispersion interferometer has been studied, and the design and analysis of different configurations have been carried out. The research has the specific goal to supply background research on the best configuration of dispersion interferometer, working towards the realization of a DI for the DTT experiment.

The Divertor Tokamak Test facility (DTT) is a project launched to investigate alternative power exhaust solutions for DEMO, a prototype for a fusion power plant. Specifically, DTT will investigate the power exhaust system, in order to work with the large energy loads expected for the divertor of a DEMO. The experiments aim to study scaled experiments integrating most of the possible aspects of the DEMO power and particle exhaust. This machine is a tokamak

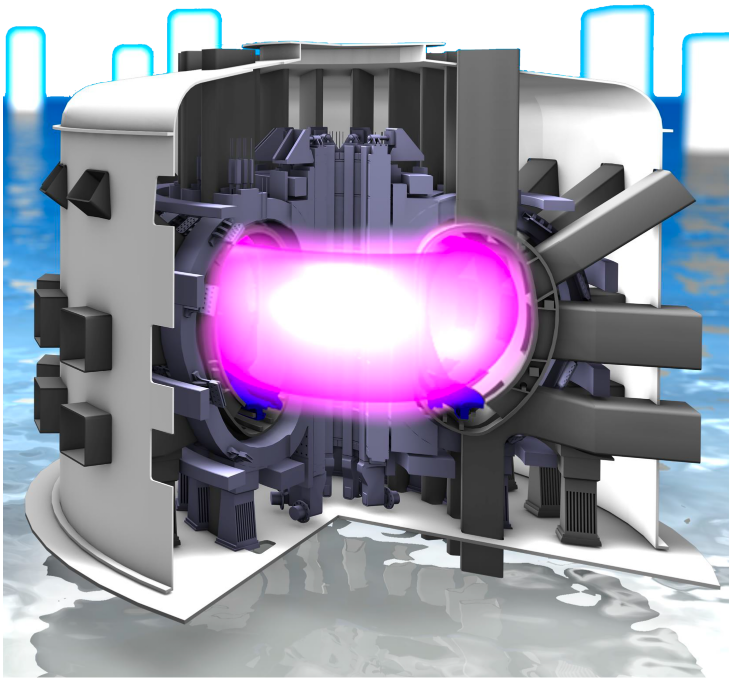

Figure 1.3: Design of DTT machine.[12]

where it will be possible to test different divertor magnetic configurations, to determine the best solution for the power exhaust problem.
In order to reach edge conditions as close as possible to DEMO, the set of parameters chosen for DTT is compatible with bulk plasma performances, and also allows having a sufficient flexibility to test a wide set of divertor concepts and techniques: conventional tungsten divertors, liquid metal divertors, both conventional and advanced magnetic configurations (including single null, snow flake, quasi snow flake, X divertor, double null), internal coils for strike point sweeping and control of the width of the SOL (Scrape-Off Layer) in the divertor region, radiation control. This experiment will focus much attention on the diagnostics and control issues, in particular in the divertor region[13].
The study on the dispersion interferometer enters the group of diagnostics that will be used for DTT.

Experimental Components

In this chapter, a summary of the experimental components used on the optical bench is exposed. Not all the described elements will be used in every configuration, but to make the reading of the following chapter easier, all the important components and their characteristics are listed here.

2.5 Optical Components

The laser used in this experiment is a Koheras ADJUSTIK single-frequency fiber-laser, shown in Fig. 2.4 (a).
Since the interferometer should work on a plasma machine, the laser control system will be far from the area of operation. It will be necessary to integrate a longer fiber[1] as the output from the laser. For this reason, a longer fiber was installed, connecting it to the output of the fiber of the laser.
A collimator[2] is then installed at the output of the fiber.

(a)

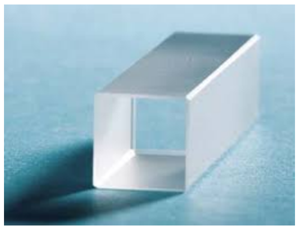

(b)

Figure 2.4: (a) Picture of the Koheras ADJUSTIK single-frequency laser; (b) Descriptive picture of the LBO crystal

The crystals used are Lithium Triborate crystals, of dimensions $10 \times 3 \times 3\ mm$ (Fig. 2.4 (b)). As described in Par.1.2, the SHG is achieved in critical phase matching conditions: the polarization of the fundamental beam needs to be aligned in the ordinary direction, and the exiting fundamental beam will maintain the same polarization, while the second harmonic beam generated will have extraordinary polarization direction, orthogonal to the fundamental beam.
To generate the second harmonic the phase matching condition must be fulfilled. As explained in Par. 1.2, Eq. 1.14 must be satisfied, ad so the input beam must impinge in the front face of the crystal orthogonally. The crystal is cut so that the beam arriving perpendicularly has the right angle θ.
In Appendix A, Fig. 7.46 it is possible to see a description of the crystal: on one of the sides,

[1] P3-1550PM-FC-5 1550 nm PANDA PM FC/APC Patch Cables.
[2] F240APC-1550 - 1550 nm, f = 8.18 mm, NA = 0.49 FC/APC Fiber Collimation Pkg.

there was a mark showing which is the correct input face of the crystal, from which it is possible to derive the direction of the polarization necessary to generate the second harmonic correctly.

To insert the crystals into the optical bench, some holders were designed and built. The first model of the holder was designed to be independent of other optical elements. The technical design of this model is shown in Appendix A, Fig. 7.47. A picture of the final product is shown in Fig. 2.5.
Each holder was mounted on a platform that could rotate around the horizontal axis.

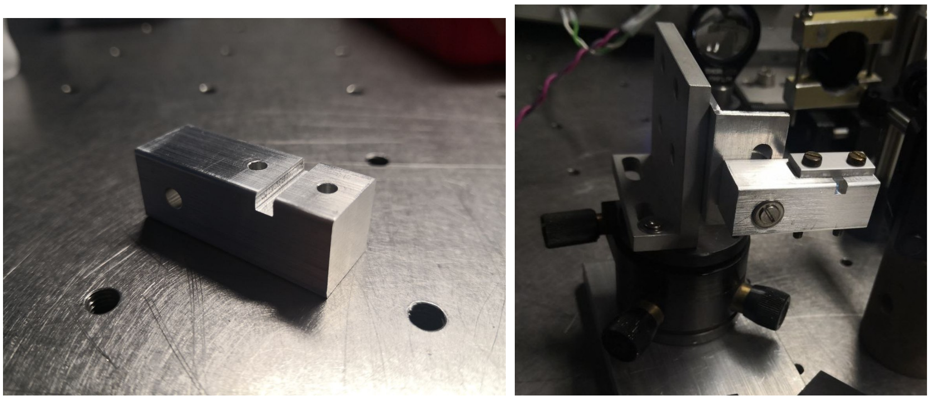

Figure 2.5: Pictures of the first crystal holder, and a picture of it mounted on the rotating platform.

Later on, a new holder was designed and built for the crystals: the necessity of a rotating degree of freedom arose, and a new model of holder was designed, in order to be able to insert the crystal inside a mirror mount, that gives the possibility to rotate the crystal. A vertical stage holding the mirror mount was also designed. The technical drawings are shown in Appendix A, Fig. 7.48. the built result is shown in Fig. 2.6.

Figure 2.6: Pictures of the second crystal holder, with the crystal inserted in it, mounted on the vertical stage, on the rotating platform.

In the setup four concave mirrors with Enhanced Silver coating[3] has been used. They were positioned before and after the crystal in order to focus the beam. Their radius of curvature is equal to 150 mm, their thickness 6 mm. All the other information can be found in [14]. To focus the beams on the detector a plano-convex lens of focal length equal to 40 mm has been inserted.

In the system, some windows have been used. The laser beams of the system pass through them, and their specific refractive index, different for each wavelength, produces a phase acquisition. These windows are mounted on a goniometric stage, so that it was possible to control the change of the optical path of the beams with respect to the impact angle between the propagation direction of the beams and the optical axis of the window so that an interference pattern could be recorded and studied. The

[3] 092-0125R-150 BK7 pl/cv mirror d25, 4×6 mm ROC=150 mm, coating Ag protected.

goniometric stage has been positioned both vertically and horizontally.
The windows used were:

- a Sapphire window, of thickness equal to 1 mm, characterized by a nominal transmittance of 80%. The refractive indices are $n_{1.55} = 1.53$ for the fundamental beam, and $n_{0.775} = 1.54$ for the SH beam;

- a Quartz Z-cut window, of thickness equal to 5 mm, and nominal transmittance 90%. The refractive indices are $n_{1.55} = 1.746$ for the fundamental beam, and $n_{0.775} = 1.761$ for the SH beam.

The transmittance has been experimentally verified, by means of measurements with a powermeter, collecting data before and after introducing the windows in the system. The measurements have been done at different angular positions of the window. The results found were an experimental transmittance of 78.8% for the Sapphire window, and of 87.6% for the Quartz one. The nominal values have thus been accepted.

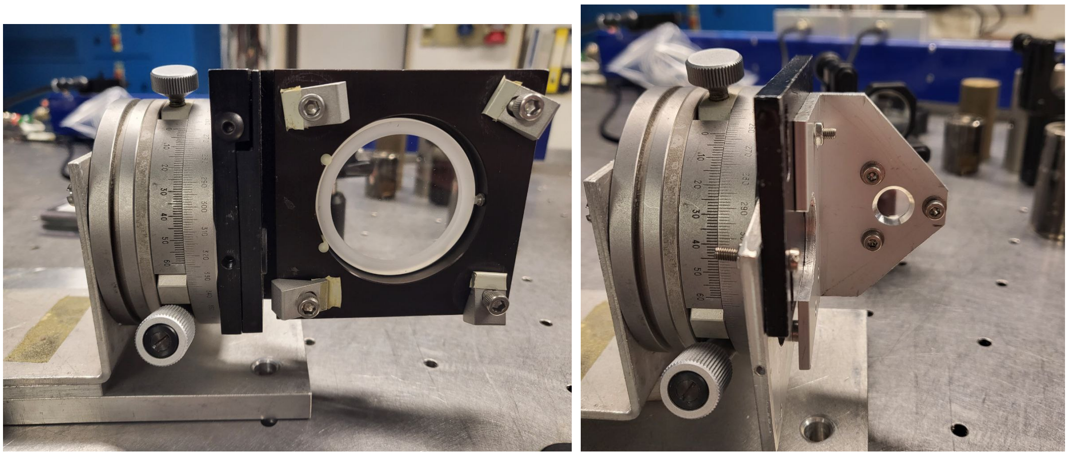

Figure 2.7: (left) Z-cut Quartz window mounted on the goniometric stage, in horizontal orientation; (right) Sapphire window mounted on the goniometric stage, in a horizontal orientation.

In a specific configuration, explained in Par. 3.2.3, a quartz half-wave plate has been used. It was an EKSMA Zero Order half-wave plate, with retardation of $\lambda/2$ at $\lambda = 0.775$ μm, AR coated, mounted into a black anodised aluminum ring with a diameter of 25 ± 0.5 mm.

To implement the heterodyne configuration, which will be explained in Par. 4.3, two Dichroic Longpass Filters[4] has been used. They transmit the fundamental beam, reflecting the SH beam. They will be used to deflect only one of the two beams, to modulate the fundamental one, and then recollect them together.

In one of the configurations, the one which uses the heterodyne technique, an acousto-optic (AO) cell is employed. Specifically, the AO cell implemented is a custom AO Frequency Shifter[5] by Brimrose, which operates at wavelength 1.55 μm, and applies a frequency shift of 40 MHz. It is driven by a Fix Frequency RF Driver[6], set at working frequency 40 MHz. The data sheet of these components is shown in Appendix A, Fig. 7.50 and 7.51. They contain all the information about the materials and the optical characteristics of the Bragg cell.

[4] Dichroic Longpass, 100 nm, 25 mm of diameter, R5000923977-22137, by Edmund Optics.
[5] Model AMF-40-20-1550/4mm
[6] Model FF-40-B1-F1

2.6 Data Acquisition

Regarding the detection of the simple interferometric signal, as for the case of the homodyne detection (Par. 3.1), a monolithic photo-diode with an on-chip transimpedence amplifier[7] has been used. The circuit has been developed by choosing a feedback resistance equal to $1M\Omega$ (Appendix A, Fig. 7.49).
The detector was connected to an oscilloscope[8]. The measured signals were visualized in Voltage units.
The associated error to the collected data has been estimated considering that the vertical resolution is characterized by 8 *bit*. The theoretical resolution is thus calculated as 0.39% of the full-scale.
It is possible to convert the voltage values into intensity values: the conversion was made following the graph in Appendix A, Fig. 7.49, estimating the power value, and from that the intensity value (with a hypothesis on the beam waist, deduced by some simulations).

Regarding the more complex heterodyne scheme detection, a demodulating system must be introduced. During the thesis work, this system has not been installed, but the components have been selected in order to set it in the next months.
The demodulating apparatus will be connected to the RF driver which powers up the Acousto Optic Modulator. The photo-diode must be changed since the one used before does not have a bandwidth high enough to acquire the modulated signal (modulation equal to 40 MHz).

[7] OPT101 Monolithic Photo-diode and Single-Supply Transimpedence Amplifier
[8] *Rohde and Schwarz* HMO3004

Homodyne Configuration

The first setup studied for the dispersion interferometer is the homodyne one.
In this scheme, the two beams which interfere fall on the same detector, and the signal collected by the detector is proportional to[15]

$$\overline{E^2} = \frac{1}{2}\ E_1^2 + \frac{1}{2}\ E_2^2 + E_1\ E_2\ cos(\Delta\phi) \tag{3.19}$$

where the first and second terms are the intensities of the two beams, and $\Delta\phi$ is the phase shift which contains information about the electron density).
This is a very simple system, which requires an easy design on the optical bench.
Some problems with this technique[16] are:

- the sign of the phase shift $\Delta\phi$ is not defined;
- when the inversion of the cosine function is made, π is a critical point;
- The measurements depend on the intensity, so power fluctuations may affect negatively the estimate.

These problems can be solved in the second scheme which will be analyzed in Chap. 4.3.

3.1 Schematic Description and Experimental Realization

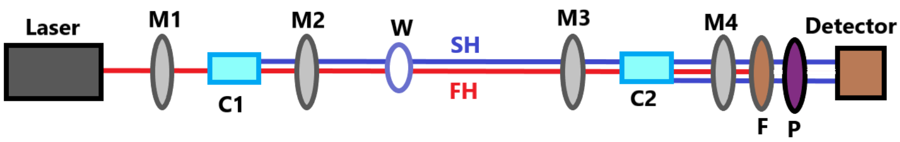

Figure 3.8: Homodyne interferometer scheme. To the left you can find the laser source; M1, M2, M3 and M4 are concave mirrors, C1 is the first LBO crystal, C2 is the second one, W is the window which simulates the plasma, F is a filter that blocks the FH beam, P is a polarizer and to the right the detector is shown.

A schematic representation of this system, which has been realized on the optical bench, is shown in Fig. 3.8. All the experimental components used have been described in Par. 1.4.
The fundamental harmonic (FH) beam is originated from the laser (provided with a collimator that produces a parallel beam). Then the first pair of mirrors (M1 and M2) focus the beam so that its Rayleigh range $z_R \simeq 5mm$; The focused beam passes through the first crystal and thus second harmonic (SH) beam is generated.
Both beams (FH beam and SH one) pass through a window (W): Two different types of windows have been inserted, one made of z-cut Quartz and one made of Sapphire (Fig. 2.7). They have been inserted to simulate the plasma, in fact, they introduce a change in the optical paths of

the beams with respect to the impact angle, because of the material dispersion.
The second pair of mirrors (M3 and M4) focus the beam analogously as before, and at the focus, the second crystal is installed, so that the remaining FH beam produces another SH beam (with a different phase with respect to the first SH beam generated). A polarizer is positioned before the detector, with an orientation that depends on the configuration. A filter that blocks the FH beam is positioned before the detector, even though the photo-diode used is not sensitive to the fundamental wavelength. The interference between the two SH beams is thus observed.

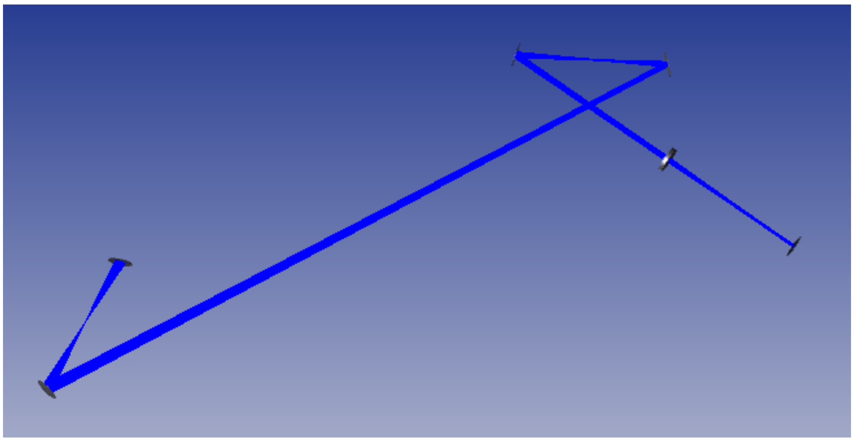

Figure 3.9: Visual scheme of the simulated beam with Zemax at its optimal configuration.

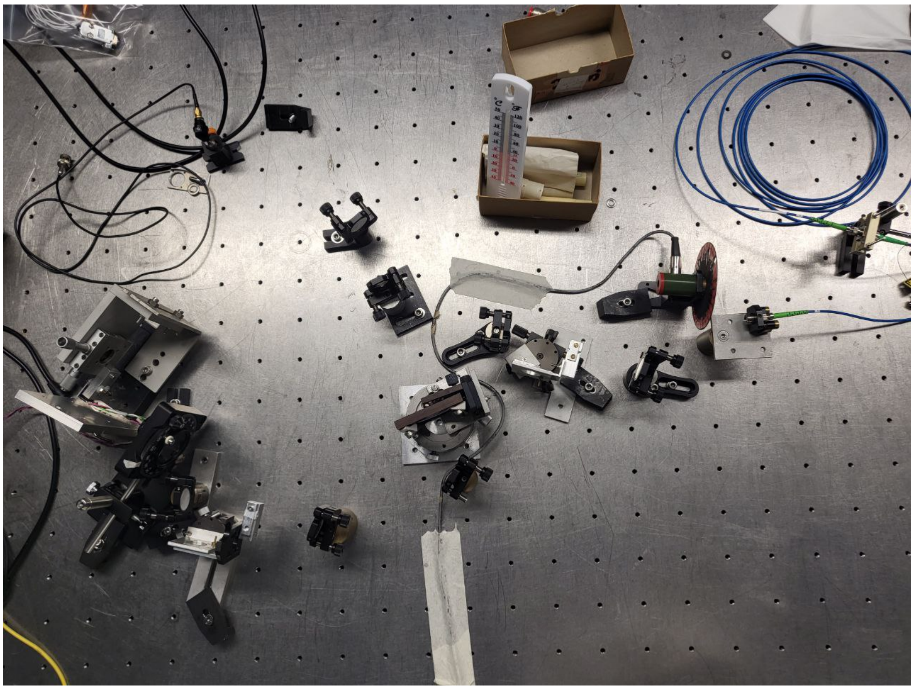

Figure 3.10: Picture of the setup on the optical bench.

This configuration has been studied through simulations carried out using the software Zemax: it is a program which offers beam simulations and gaussian analysis, modeling gaussian beams and reporting various beam data, including beam size and waist location as it propagates through a paraxial optical system.
The goal was to optimize the setup, changing the position of the mirrors, to achieve a Rayleigth range z_R equal to 5 mm, which is half the crystal length. This is a compromise to have a small

waist but not a very divergent beam: without this condition the length of the crystal would not be exploited at its best for the SHG.
This condition to optimize the power density of the beam inside the crystal can be translated in a condition on the waist: a beam waist value near 47.5 μm corresponds to $z_R = 5\ mm$.
The best configuration to achieve this condition on the waist using the four concave mirrors is shown in Fig. 3.9.
The pairs of concave mirrors (M1 and M2, and then M3 and M4 from Fig. 3.8) were positioned 15 cm from one another. This value is the curvature radius of the mirrors.
The distance between M2 (the second concave mirror of the first pair) and M3 (the first mirror of the second pair) is 70 cm, and because of the chosen configuration, along this path, the beam propagates with an almost constant waist. This distance was chosen to have enough room to insert the various optical elements needed.

The resulting optimization has been implemented on the optical bench. The experimental setup is shown in Fig. 3.10.

During the homodyne scheme experimentation, the crystals used to generate the second harmonic beams have been positioned with three different orientations:

- At first both crystals were positioned with the ordinary axis parallel to the FH beam polarization. This orientation was the one that guarantees the best efficiency of SHG, since the polarization of the FH beam is vertical, and it matches with the ordinary axis of both the crystals. The problem observed with this setup is that the SH beam generated by the first crystal has the same polarization as the one generated in the second one, and during this second SHG there could be a nonlinear dependence of the intensity generated, and the interference pattern is not the expected one. To overcome this, a second setup has been implemented.
- In the second setup, the first crystal is oriented with the angle between the ordinary axis and the FH beam polarization of 45°, and the second crystal orthogonal to that, so the two SH beams generated have orthogonal polarization and the SHG generated in the second crystal is independent of the first SH beam. The polarizer positioned before the detector with a fixed orientation allows the interference of the two SH beams.
- At last the crystals were positioned back again in the first horizontal orientation, but a half-wave plate has been inserted after the first crystal, to rotate the SH beam polarization of 90°. The half-wave plate should theoretically act as a full-wave plate for the fundamental beam, leaving its polarization unchanged, despite the dispersion of its material. In this way, the half-wave plate rotated the SH beam generated by the first crystal so that it has a polarization orthogonal to the one of the SH beam generated in the second crystal, which is the same, given that the orientation of the second crystal is the same as the first one. This configuration should be conceptually equivalent to the second one.

The windows (W) are mounted on a goniometric stage so that changing their angle corresponds to modifying the optical path inside the window for the two beams. The collected intensity can be expressed with respect to the optical path difference ($\Delta\varphi$): The relation expected follows the equation:

$$I = I_1 + I_2 + 2\sqrt{I_1 I_2} cos(\Delta\phi) \tag{3.20}$$

This equation is valid in the case when the two generated beams are generated independently, and this is why the second and third configurations have been introduced.
In the next paragraphs, the different results obtained for the homodyne configurations are shown and analyzed.

3.2 Data Collection and Analysis

As explained in the previous paragraph, the feasibility of the instrument has been analyzed inserting a rotating window, to simulate the plasma, after the first crystal.
The presence of the window along the optical path of the beams causes a phase difference. This added phase is related to the change of the optical path caused by the travel of the beam through the dispersive material.
The fact that the fundamental beam acquires a certain phase travelling through the window, while the second harmonic acquires a different phase, because of its different wavelength, allows you to measure an interferometric signal due to the superposition of the first SH beam and the one converted by the second crystal.
Right after the collimator, a chopper has been installed: its function is to better measure the signal as a step signal on the background.
The data acquisition has been carried out by collecting the values of the total intensity, measured as voltage by the photo-diode for various angles of the window, visualizing on the oscilloscope.
It is possible to write a relation between θ (the angle between the direction of the beams impinging on the window and optical axis of the window) and the optical path crossed by the beams inside the window.
From the optical path it is, then, possible to estimate the phase shift of the beams.

In Eq. 3.20 the equation related to the total intensity detected on the photo-diode is shown. Specifically, considering that the two beams are the fundamental one (characterized by a frequency ω) and the respective second harmonic beam (with frequency 2ω), the phase difference $\Delta\phi$ present in the equation can be written as

$$\Delta\phi = 2\phi_F - \phi_{SH} = \frac{2\omega}{c}\int [n(\omega) - n(2\omega)]\ dl \simeq \frac{2\omega}{c}[n(\omega) - n(2\omega)]\,R \tag{3.21}$$

where ω is the frequency of the fundamental beam, $n(\omega)$ is the refractive index for the wavelength of the fundamental beam while $n(2\omega)$ for the second harmonic beam and R is the optical path.
As a first analysis, a simplified equation has been used to evaluate the optical path and the subsequent phase change of the beams in the material of the window. The beams are suppose to travel through the window without deviating. The equation for this approximation is

$$R_{simpl} = \frac{d}{cos\theta} \tag{3.22}$$

where d is the thickness of the window and θ is the angle between the incoming beams and the optical axis of the window, as shown in Fig. 3.12.
Secondly, a more complex equation has been used, where the Snell law has been taken into account. The equation for the optical path is

$$R_{Snell} = \frac{d}{cos\left(arcsin\left(\frac{1}{n}sin\theta\right)\right)} \tag{3.23}$$

where a dependence on the refractive index n of the material of the window has been added.
The explanatory description for this approximation is shown in Fig. 3.13.
these two equations for the optical path R have been inserted in Eq. 3.20. The respective functions of the total intensity with respect to the angle θ have been plotted and are shown in Fig. 3.11.
These functions are the ones which will be used as a comparison for the experimental values collected.

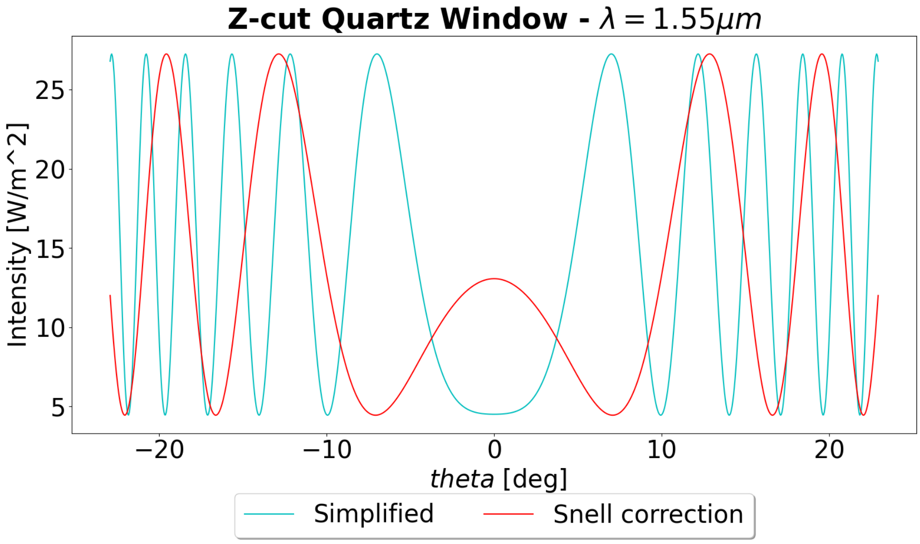

Figure 3.11: Plot of the intensity function with respect to the angle θ. The equations have been evaluated using the characteristic values for a Z-cut Quartz window, as the one used in the experimental setup, and considering the fundamental beam with a wavelength 1.55 μm (and the respective second harmonic beam of 0.775 μm).

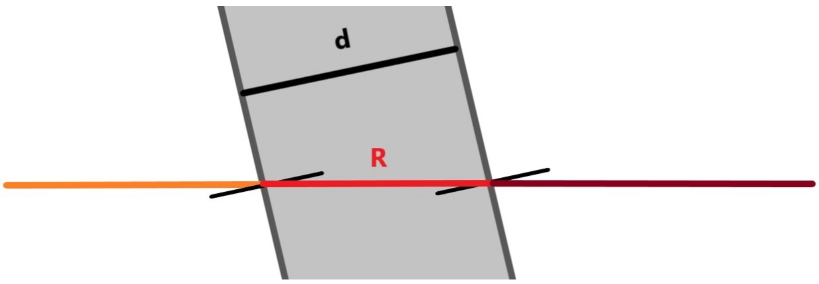

Figure 3.12: Schematic description of the estimate of the optical path inside the window in the simplified treatment which evaluates $R = R_{simpl}$ (Eq. 3.22); d stands for the thickness of the window.

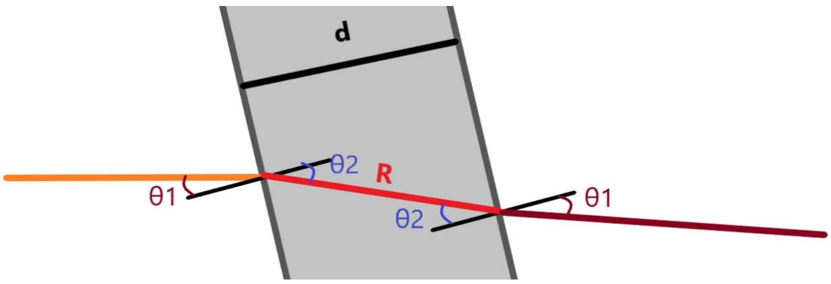

Figure 3.13: Schematic description of the estimate of the optical path inside the window considering the Snell law which evaluates $R = R_{snell}$ (Eq. 3.23); d stands for the thickness of the window.

3.2.1 Parallel Configuration

In this configuration, both crystals were positioned horizontally, with the ordinary axis parallel to the fundamental beam polarization. As said before, this orientation guarantees the best efficiency of SHG.
For this configuration, the first type of crystal holder (Fig. 2.5) has been used. It represented a good choice since its natural structure is well designed to hold the crystal horizontally.

The holder has been positioned on the rotating platform, given different degrees of freedom to adjust the crystal position in order to achieve the phase-matching condition.
The first crystal has been inserted first, and the configuration has been optimized until the SH generated was as high as we could get it.
Then the same optimization has been done for the second crystal. The two SH beams have been checked using two filters: to collect the SH signal from the first crystal, a filter that blocks the fundamental beam was positioned before the second crystal; to visualize the signal from the second crystal, a filter that blocks the beam at 0.775 μm has been positioned instead.
As expected, the SH beam obtained from the first crystal was always higher than the one from the second crystal. Confronting other experiences in SHG, it appears that, passing through the first crystal, the fundamental beam is subject to some degradation so that the conversion at the second crystal never achieves the same efficiency of generation.

The data acquisition was carried by setting a certain value for the rotational position of the window, with the precision of $1/60\ deg = 0.00029 rad = 1\ min$. Then the value of the peaked signal observed on the oscilloscope was recorded.
Different data-sets were collected, in order to determine the best range of data to represent the interferometric signal.
The reproducibility of the data was not great, since the window was re-positioned many times due to adjustments to the setup. Each time the value of the perpendicular position of the window with respect to the incoming beams was redefined. This value was not easy to determine, and this could cause a variation in the optical paths computation.

Numerous data-sets have been collected, because it was initially necessary to select the right range of acquisition in order to see two consecutive maxima or minima.
The three best data-sets chosen for this configuration are now shown (Tab. 3.1). These are the ones that better resemble the theoretical equation of the interferometric signal.

Data-Set	**Window**	**Crystals orientation**	V_1	V_2	$V_1 + V_2$	$2\sqrt{V_1 V_2}$
17	Quartz	in parallel	190 mV	178 mV	368 mV	367.8mV
23	Quartz	in parallel	190 mV	178 mV	368 mV	367.8mV
7	Sapphire	in parallel	/	/	/	/

Table 3.1

In Tab. 3.1 the voltage values of the SH signal from the first crystal, V_1, and the SH signal from the second crystal, V_2, are shown. They were collected using the filters, as explained in this paragraph before.
These values were used in order to understand if the values of the parameters found fitting the theoretical function with the experimental data was in accord or not.
The values for data-set 7 were not collected.

The voltage data collected as a function of the angle θ have been fitted with the equation

$$V(\theta) = A + B\ cos\left(\frac{2\omega}{c}\left[n(\omega) - n(2\omega)\right]\frac{d}{cos(\theta + \phi)} + C\right) \tag{3.24}$$

where A, B, ψ and C are the parameters with respect to which the fit has been optimized. A is related to the value $V_1 + V_2$, B to $2\sqrt{V_1 V_2}$, ψ represents ad additional angle to the incident one, which has been introduced to take into account a possible misalignment of the window on

the rotating structure and C is an additional phase that may be related to the optical effects of the other optical elements the beams pass through other than the window.
This equation corresponds to the simplification deriving from considering the optical path equation equal to Eq. 3.22.
The fit did not converge, since the expected curve showed some nonlinear dependence on the sinusoidal.
A second function has been used to compare the experimental data, exposing the voltage as a function of the phase shift calculated from the angle θ with Eq. 3.21 and 3.22:

$$U(\Delta\phi) = \tilde{A} + 2\tilde{B}\ cos\left(\Delta\phi\ \tilde{C} + \tilde{\psi}\right) \tag{3.25}$$

where $\Delta\phi$ was evaluated as explained in Eq. 3.21 with the simplified optical path (Eq. 3.22), and $\tilde{A}$, $\tilde{B}$, $\tilde{\psi}$ and $\tilde{C}$ are the parameters with respect to which the optimization is carried out. Again $\tilde{A}$ is related to the value $V_1 + V_2$, while $\tilde{B}$ to $\sqrt{V_1 V_2}$. As before, the parameters $\tilde{\psi}$ and $\tilde{C}$ are inserted to take into account the possible misalignment of the window and the phase shift related to the other optical elements.
The resulting function has been optimized to describe the experimental data, and it was plotted together with the data, and shown in Fig. 3.15 and 3.14.
The parameters obtained in the optimization are shown in Tab. 3.2.

Data-Set	**Window**	$\tilde{A}$	$\tilde{B}$	$\tilde{\psi}$	$\tilde{C}$
17	Quartz	222 mV	46 mV	25.5	0.23
23	Quartz	248 mV	50 mV	46	0.19
7	Sapphire	255 mV	25 mV	16	11

Table 3.2

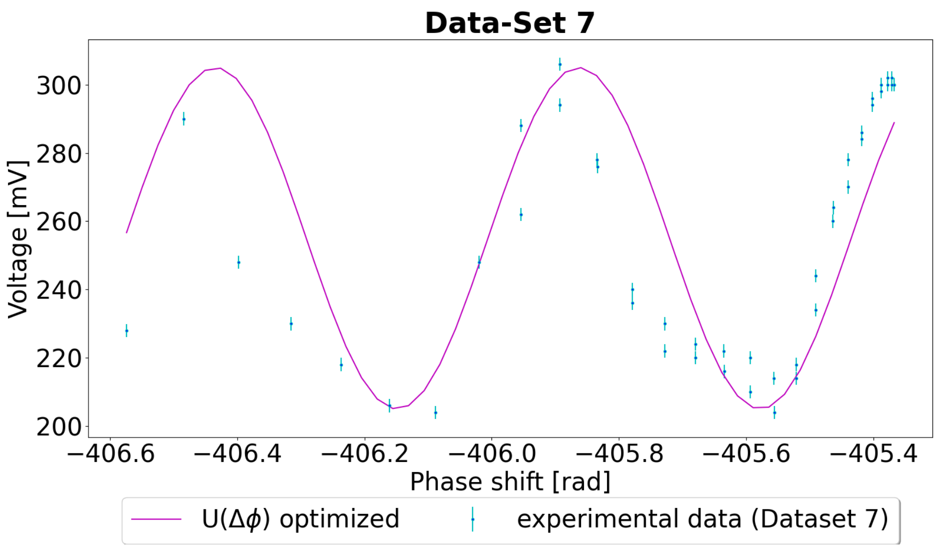

Figure 3.14: Experimental data for the Data-Set 7 (crystals positioned in parallel, Sapphire window), shown as a function of the phase shift, computed from the angle θ between the incoming beams and the window optical axis; superimposed on the data, the optimized function $U(\Delta\phi)$ (Eq. 3.25) is shown. The full-scale used during the data acquisition on the oscilloscope is equal to 50 mV, which implies an error equal to $\pm 1.95\ mV$ on the voltage measures (calculated as explained in Par. 2.6).

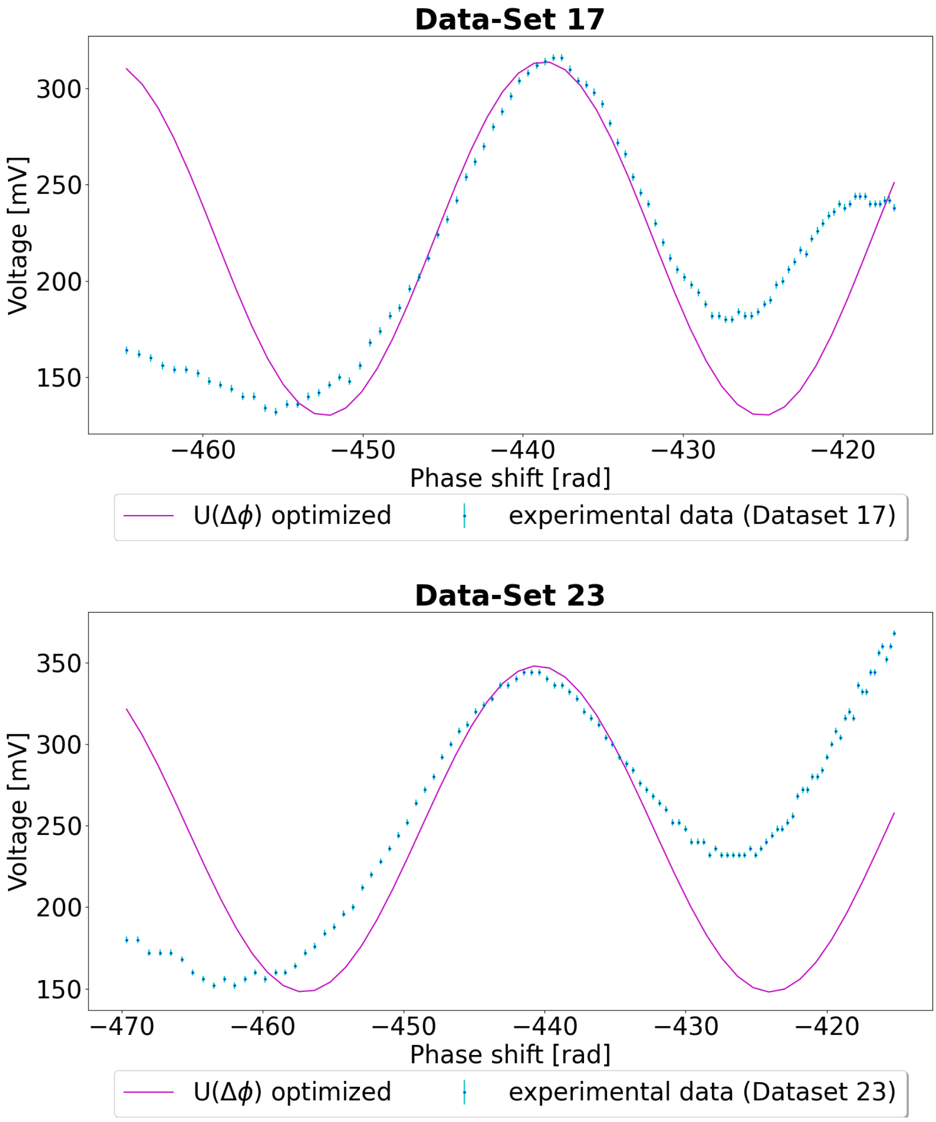

Figure 3.15: Experimental data for the Data-Set 17 and 23 (crystals positioned in parallel, Quartz window), shown as a function of the phase shift, computed from the angle θ between the incoming beams and the window optical axis; superimposed on the data, the optimized function $U(\Delta\phi)$ (Eq. 3.25) is shown. The full-scale used during the data acquisition on the oscilloscope is equal to 50 mV, which implies an error equal to ± 1.95 mV on the voltage measures (calculated as explained in Par. 2.6).

Confronting the values obtained in the fit for $\tilde{A}$ and $\tilde{B}$ (Tab. 3.2) with the values of $V_1 + V_2$ and $2\sqrt{V_1 V_2}$ evaluated from the pure signals of SH beams, shown in Tab. 3.1, it is possible to see that the fitted function is very far from the theoretical description, for all three sets.

While the data-sets 17 and 23, where the Quartz window was used, were at least describing a sinusoidal function, even though with parameters different to the one predicted, the data-set 7 was far off. The problem was identified in the Sapphire window, whose high value of the refraction index may introduce a considerable amount of internal reflections.
For this reason, from this point on, the data collection has been carried out using the Quartz window.

Overall, this parallel configuration was not well described by the theoretical description adopted.

A reason for this is that the SH beam generated by the first crystal has the same polarization as the one generated in the second one, and during this second SH generation, there could be a nonlinear dependence from the first. The beating of the signals could have generated some modulations. For this reason, the interference pattern is not the expected one. This effect is responsible for a more complex relation of the voltage with the angle θ, and so it is not possible to reconstruct an equation for the interferometric signal.

To overcome this problem, a second setup has been implemented, where the polarization of the first generated SH beam is orthogonal to the one of the SH beam generated in the second crystal.

3.2.2 Orthogonal Polarization Configuration

A new configuration has been studied, to solve the problem which arises from the two SH beams having the same polarization inside the second crystal.
In the new configuration, one crystal is oriented with the angle between the ordinary axis and the FH beam polarization of 45°, and the second crystal orthogonal to that, so the two SH beam generated have orthogonal polarization and the SHG produced by the second crystal is independent from the first SH beam.
To recollect the interferometric signal a polarizer was positioned before the detector: it was regulated in order to let pass only the vertical polarization, intercepting both the polarizations of the SH beams, creating the interference, which would be described in Eq. 3.20.

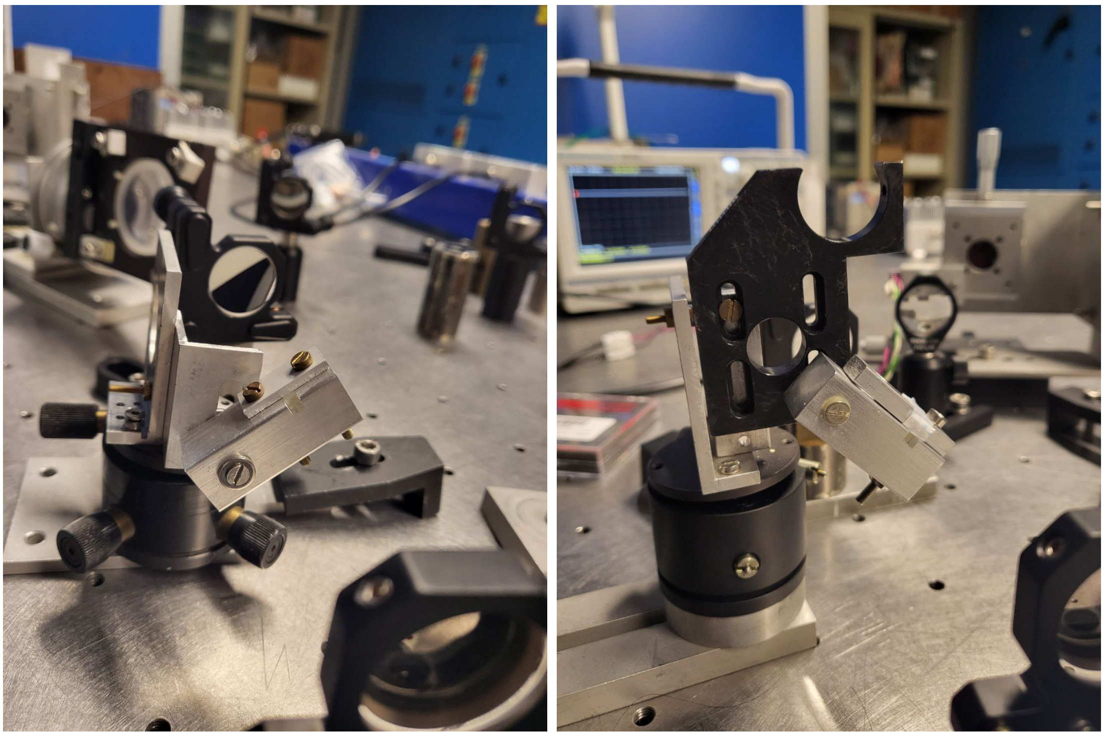

Figure 3.16: (left) picture of the first crystal positioned at 45° with respect to the vertical direction, mounted on the first crystal holder; (right) picture of the second crystal, positioned at 45° with respect to the vertical direction, and orthogonal to the first crystal, on the first crystal holder.

At first, the configuration has been achieved using the same crystal holders as before. They have been described in section 1.4, and are shown in Fig. 2.5. These holders were originally designed to position the crystals in the horizontal position, but they were used anyway for this configuration, while waiting for the realization of the new holders.

Two pictures of this configuration are shown in Fig. 3.16.

The two best data-sets chosen for this configuration are now shown (Tab. 3.3). Again the values of the voltage measured for the beams produced in the two crystals were collected independently, and the values are shown in the same table.

Data-Set	**Window**	**Crystals orientation**	V_1	V_2	$V_1 + V_2$	$2\sqrt{V_1 V_2}$
30	Quartz	orthogonal	19.2 mV	10.4 mV	29.6 mV	28.3mV
31	Quartz	orthogonal	19.2 mV	10.4 mV	29.6 mV	28.3mV

Table 3.3

The voltage data collected with respect to the angle θ have been fitted with Eq. 3.24. The resulting values of the parameters are shown in Tab. 3.4. The fitted equation has been plotted alongside the experimental data, shown as a function of the phase shift calculated from the angle θ using Eq. 3.21 and 3.22, and the graph is shown in Fig. 3.17 and 3.18.

Data-Set	**Window**	A	B	ϕ	C
30	Quartz	38.7 mV	15.4 mV	0.008	-3.8
31	Quartz	35.0 mV	12.4 mV	0.008	2.7

Table 3.4

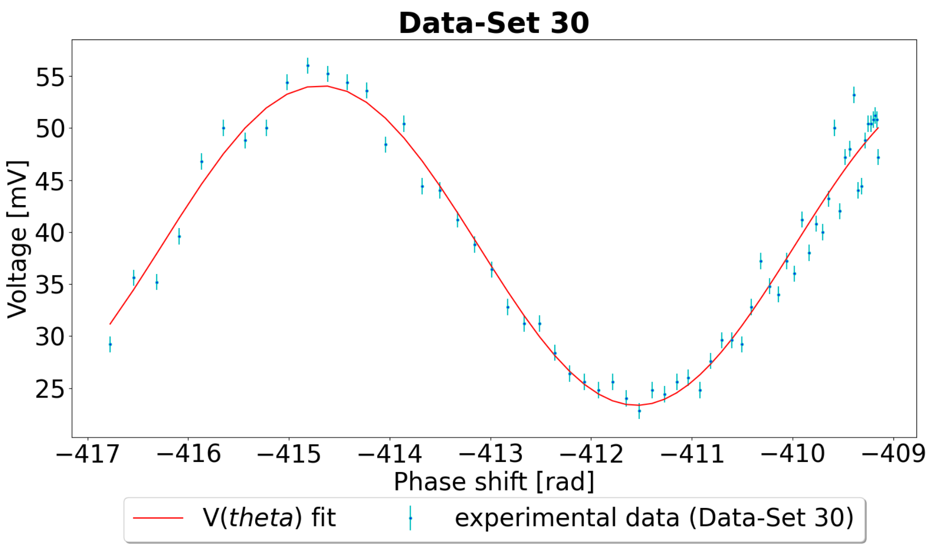

Figure 3.17: Experimental data for the Data-Set 30 (crystals positioned orthogonally, Quartz window), shown as a function of the phase shift, computed from the angle θ between the incoming beams and the window optical axis; superimposed on the data, the fitted function $V(\theta)$ (Eq. 3.24) is shown. The full-scale used during the data acquisition on the oscilloscope is equal to 20 mV, which implies an error equal to ± 0.78 mV on the voltage measures (calculated as explained in Par. 2.6).

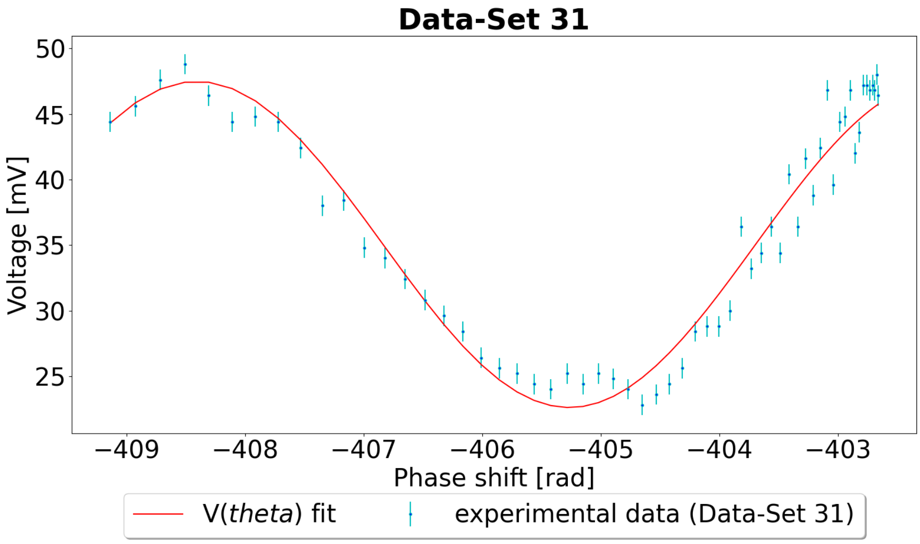

Figure 3.18: Experimental data for the Data-Set 31 (crystals positioned orthogonally, Quartz window), shown as a function of the phase shift, computed from the angle θ between the incoming beams and the window optical axis; superimposed on the data, the fitted function $V(\theta)$ (Eq. 3.24) is shown. The full-scale used during the data acquisition on the oscilloscope is equal to 20 mV, which implies an error equal to ± 0.78 mV on the voltage measures (calculated as explained in Par. 2.6).

Comparing the values of the parameter A (Tab. 3.4) with the quantity $V_1 + V_2$ (Tab. 3.3), it is possible to see that, even if there is some deviation from the theoretical values, the accordance is much better than the previous configuration. The order of magnitude is the same, and there is a difference of about 10 mV between the fitted parameters and the quantities evaluated from the pure voltages.
These discrepancies may be related to some facts: the quantities reported in Tab. 3.3 have been collected with the presence of the filters, positioned to block one of the SH beams at a time. They could have had some absorption effects on the beams. Regarding the data collected shown in Fig.3.17 and 3.18, to collect them the window was positioned in the path of the beams: the window may cause absorption and deviation of the beams. We should also take into account the fact that the crystals may not be positioned at exactly 45° with the vertical direction. This could explain the lower value presented in Tab. 3.4 with respect to Tab. 3.3.
There could also be some errors in the evaluation of the optical path from the value of the angle θ. This value is in fact known with great precision, since the goniometric stage has the precision of $0.00029 rad$, but the window may not be perfectly aligned with the center of the stage, causing a difference between the actual angle and the one read on the stage.

Since this data-set is promising, a second fit was carried out, considering the equation

$$\begin{aligned} V_{Snell}(\theta) = \; & \hat{A} + \\ & + \hat{B}\; cos\left(\frac{2\omega}{c}\left[\frac{d}{n(\omega)cos(arcsin(\frac{1}{n(\omega)}sin\theta + \hat{\phi}))} - \frac{d}{n(2\omega)cos(arcsin(\frac{1}{n(2\omega)}sin\theta + \hat{\phi}))}\right] + \hat{C}\right) \end{aligned} \tag{3.26}$$

where $\hat{A}$, $\hat{B}$, $\hat{\psi}$ and $\hat{C}$ are the parameters with respect to which the fit has been optimized. $\hat{A}$ is related to the value $V_1 + V_2$, $\hat{B}$ to $2\sqrt{V_1 V_2}$, $\hat{\phi}$ represents ad additional angle to the incident one, which has been introduced to take into account a possible misalignment of the window on the rotating structure and $\hat{C}$ is an additional phase that may be related to the optical effects of

the other optical elements the beams pass through other than the window.
This equation derives from considering the optical path equation equal to Eq. 3.23. The resulting values of the parameters are shown in Tab. 3.5. The fitted equation has been plotted alongside the experimental data, and the graph is shown in Fig. 3.19.

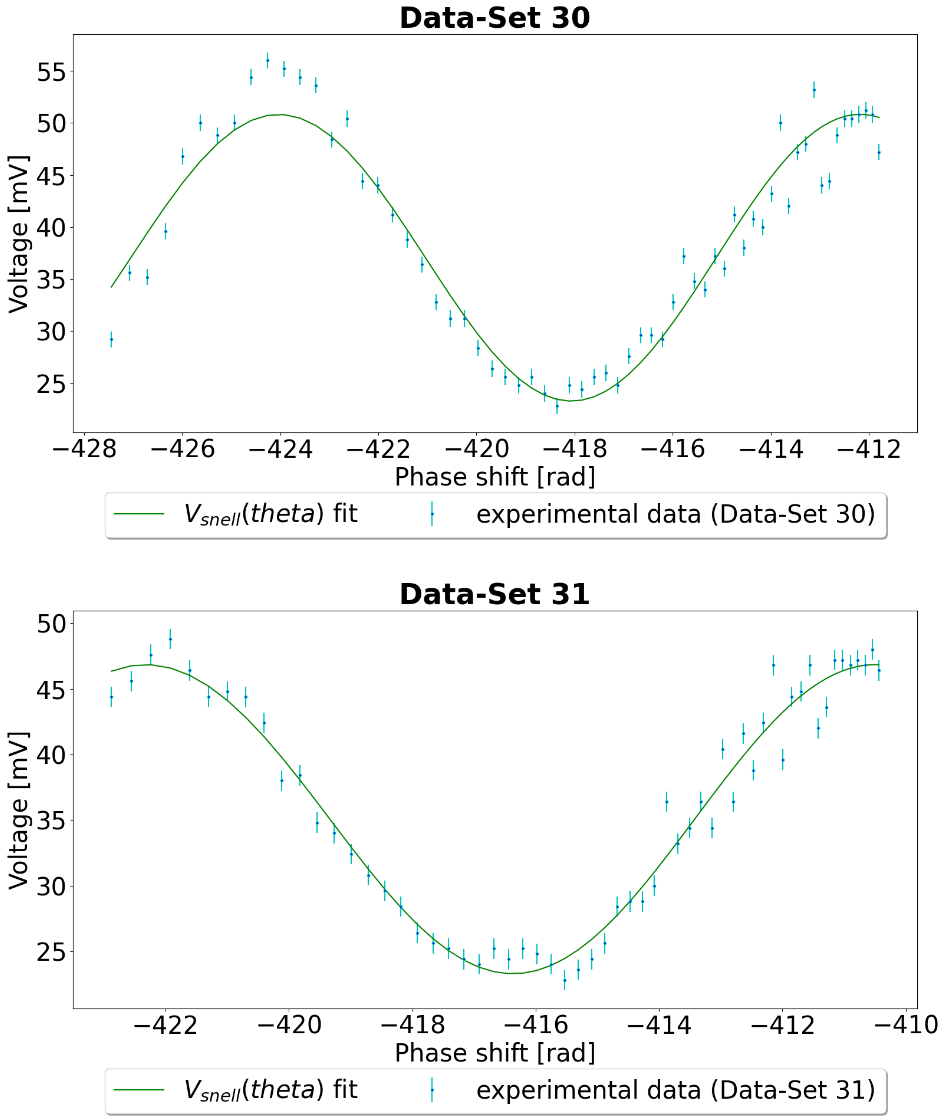

Figure 3.19: Experimental data for the Data-Set 30 and 31 (crystals positioned orthogonally, Quartz window), shown as a function of the phase shift, computed from the angle θ between the incoming beams and the window optical axis; superimposed on the data, the fitted function $V(\theta)$ (Eq. 3.26) is shown. The full-scale used during the data acquisition on the oscilloscope is equal to 20 mV, which implies an error equal to ± 0.78 mV on the voltage measures (calculated as explained in Par. 2.6).

Data-Set	**Window**	$\hat{A}$	$\hat{B}$	$\hat{\phi}$	$\hat{C}$
30	Quartz	38.1 mV	13.8 mV	0.1	-3.9
31	Quartz	35.0 mV	11.7 mV	0.09	-0.2

Table 3.5

The results are not appreciably different. This proves that there is not a big deviation of the beams passing through the window. This can, thus, be excluded from the reasons for the difference between the expected values sown in Tab. 3.3 and the fitted values of $\hat{A}$ and $\hat{B}$.

Since the crystal holders were not properly designed to work at an oriented angle, a new type of holders was built. They are shown in Fig. 2.6.
They were designed to be more conform to be oriented at a certain angle, to work better in this configuration.

Once the crystals were fixed inside the new holders, we proceeded to insert the first crystal on the optical bench. The crystal was oriented at approximately 45° with respect to the vertical direction.
The polarizer positioned before the detector was set in order to let pass only the polarization at exactly 45° with respect to the vertical direction. The polarization direction of the polarizer had been checked to be sure it was correct, and working for $\lambda = 0.775$ μm.
The holder was thus rotated accurately until the maximum value of signal was collected on the photo-diode.
Once the first crystal was set, we continued with the same method for the second crystal, focusing only on the signal from it, having positioned the filter which blocks the SH beam before it.

With this new setup, similar measurements as before have been recorded.
The best data-set chosen for this configuration is now shown (Tab.3.6).

Data-Set	**Window**	**Crystals orientation**	V_1	V_2	$V_1 + V_2$	$2\sqrt{V_1 V_2}$
37	Quartz	orthogonal	25.2 mV	10.0 mV	35.2 mV	31.7mV

Table 3.6

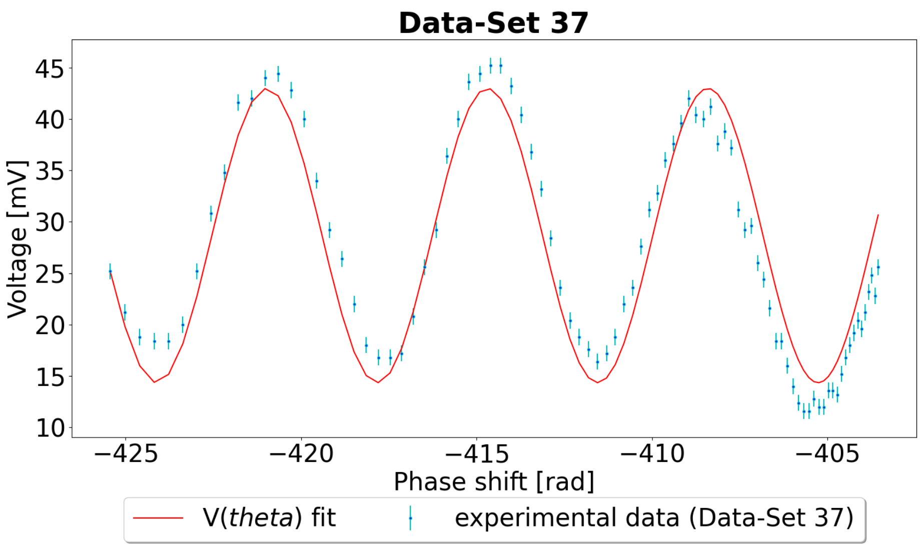

Figure 3.20: Experimental data for the Data-Set 37 (crystals positioned orthogonally, Quartz window), shown as a function of the phase shift, computed from the angle θ between the incoming beams and the window optical axis; superimposed on the data, the fitted function $V(\theta)$ (Eq. 3.24) is shown. The full-scale used during the data acquisition on the oscilloscope is equal to 20 mV, which implies an error equal to ± 0.78 mV on the voltage measures (calculated as explained in Par. 2.6).

The voltage data collected have been fitted with Eq. 3.24, obtaining the results shown in Tab. 3.7. The fitted equation has been plotted alongside the experimental data, and the graph is shown in Fig. 3.20.

Data-Set	**Window**	A	B	ϕ	C
37	Quartz	28.7 mV	14.3 mV	-0.040	2.9

Table 3.7

Comparing the values of the parameter A (Tab. 3.7) with the quantity $V_1 + V_2$ (Tab. 3.6), it is possible to see that, even if there is some deviation from the theoretical values, the accordance is again very good. The order of magnitude is the same, and there is a difference of about 10 mV between the fitted parameters and the quantities evaluated from the pure voltages.
As said for the data-sets 30 and 33, the discrepancies observed may be related to power absorption of the filters in contrast with the absorption and deviation which may be caused by the window. The window may also be misaligned on the stage.

This data-set was again fitted also with Eq. 3.26, where the Snell law effects are considered. As before, the results were not showing an appreciable difference. It was concluded that the deviation of the beams due to the window does not have a big impact on the result. This deviation must be negligible.

Overall, this configuration shows a good agreement with the theoretical behaviour expected. Rotating the crystals so that the polarizations of the two SH beams are orthogonal has been a good solution and has brought back the expected behaviour for the interference pattern.

3.2.3 Configuration with the Half-Wave Plate

Given the good result for the previous configuration, a different approach was tried in order to obtain a similar result without rotating the crystals.
Rotating them, in fact, reduces noticeably the power of the SH generated, since only the component of the fundamental beam with polarization oriented along the ordinary axis produced SH.
The crystals were positioned back again in the first horizontal orientation, and a half-wave plate has been inserted after the first crystal. In this way, the half-wave plate rotates by 90° the SH beam generated by the first crystal, so that it has a polarization orthogonal to that of the SH beam generated in the second crystal.
Ideally, the half-wave should rotate the polarization of the SH beam of 90°, leaving the polarization of the fundamental beam unchanged.
To recollect the interferometric signal, the polarizer was positioned before the detector: it was oriented in order to let pass only the vertical polarization, intercepting both the polarizations of the SH beams, creating the interference, which would be described by Eq. 3.20. As said before, the fundamental beam is cancelled with a filter, even though it is not collected by the detector.
The configuration has been achieved using the crystal holders described in section 1.4, shown in Fig. 2.5.

Before inserting the half-wave plate in the configuration just explained, its effect on the SH and the F beams was checked.
At first, only the first crystal was left on the optical bench. Then the polarized has been inserted before the photodiode, setting it at the horizontal polarization (the one for which the SH beam

observed is higher).
The half-wave plate is inserted *before* the first crystal. Rotating the half-wave plate, if it does not have any effect on the polarization of the fundamental beam, we should not see any change in the SH beam produced.
Unfortunately, this was not the case: rotating it, leaving every other optical component fixed, the SH beam observed before experienced variations.
This result implies that the half-wave plate available affects the fundamental beam too.

Secondly, we wanted to check if the fact that the fundamental beam arrives at the crystal with different polarizations implies that the SH beam polarization is different.
This should not be the case, since theoretically the non-linear medium should work with a fixed polarization of SHG. The SH should be generated along the extraordinary direction of the crystal, even though the fundamental beam arrives at different polarizations. Only the polarization component of the FH beam parallel to the ordinary axis of the crystal is responsible for SHG.
For different orientations of the half-wave plate placed before the crystal, which changes the polarization of the fundamental beam, the polarizator has been moved in order to check the maximum voltage collected for the SH beam. The maximum corresponds to the polarization of the SH beam.
The SH beam is found to have always the same polarization, as expected.

Now, it is necessary to position the half-wave plate in order to rotate by 90° the polarization of the SH beam generated by the first crystal.
The polarizer has been rotated in order to transmit the vertical polarization. The half-wave plate has been positioned *after* the first crystal. The plate was rotated until a maximum value of SH beam was detected on the photo-diode, with that configuration of the polarizer. This corresponds to seeing a SH beam polarized vertically (90° rotated with respect to the original configuration).

Finally, the second crystal was inserted and the SH beam produced by it was optimized.
The polarization of the fundamental beam arriving at the second crystal is not known, since the half-wave plate changed it, but it is known that, whatever the polarization of the F beam, the SH beam generated by the second crystal will have polarization along the extraordinary axis of the crystal.

After the optimization, the polarizer has been positioned in order to let pass the polarization in the middle between the two SH beams, as to observe the interference pattern.

With this new setup, analogous measurements as before have been recorded.
The best data-set chosen for this configuration is shown in Tab. 3.8.

Data-Set	**Window**	**Crystals orientation**	V_1	V_2	$V_1 + V_2$	$2\sqrt{V_1 V_2}$
33	Quartz	in parallel with half-wavelength plate	62.4 mV	16.0 mV	78.4 mV	63.2mV

Table 3.8

The voltage data collected have been fitted with Eq. 3.24. The fit did not converge to a meaningful result, since the expected curve shows some nonlinear dependence on the sinusoidal. The experimental data are shown in Fig. 3.21, alongside the fit, which does not express much

meaning.
The reason for that is identified with the fact that the half-wave plate causes some undetermined effects of both waves, causing the interference not to follow the expected pattern.

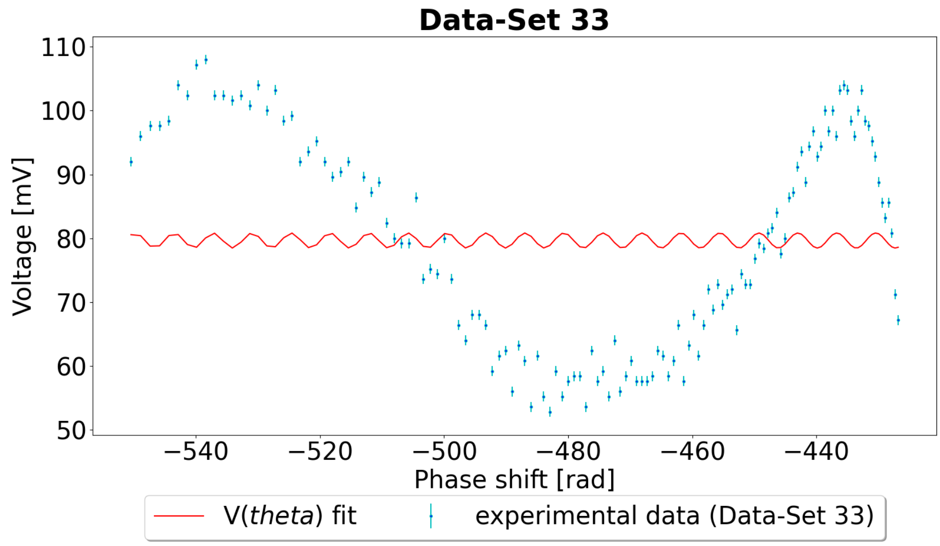

Figure 3.21: Experimental data for the Data-Set 33 (crystals positioned in parallel, with the half-wavelength plate, Quartz window), shown as a function of the phase shift, computed from the angle θ between the incoming beams and the window optical axis; superimposed on the data, the fitted function $V(\theta)$ (Eq. 3.24) is shown. The full-scale used during the data acquisition on the oscilloscope is equal to 20 mV, which implies an error equal to ± 0.78 mV on the voltage measures (calculated as explained in Par. 2.6).

This configuration is promising since it is a quite simple solution for the rotation of the polarization of one of the two SH beams. Further studies may be carried out in the future, in order to improve this configuration, for example introducing a half-wave plate for the SH beam which actually works as a full-wave plate for the FH beam. This may overcome the obstacles observed with these results.

3.2.4 Sensitivity of the Instrument

After having determined the best configuration for the homodyne setup, the interest was to obtain an estimate of the sensitivity reachable with this instrument for measurements of electron line density.
In Fig. 3.22 it is possible to observe the theoretical dependence of the voltage, which represents a measurement of the intensity recorded by the photo-diode, with respect to the optical path $\Delta\phi$, as shown in Eq. 3.21.
At the mid-fringe position, which in the graph is marked with a star, the intensity change ΔI (at which corresponds a voltage change ΔV), and the optical path change $\Delta\psi$, are proportional to each other[17].

The equation which relates the voltage values with the optical path in Fig. 3.22 is

$$V(\psi) = A + Bcos(\psi) \tag{3.27}$$

where ψ is the optical path (previously called $\Delta\psi$, here renamed not to confuse with the concept of change associated to Δ in this paragraph), $V_{max} = A+B$ and $Vmin = A-B$. Re-normalizing the Eq. 3.27 we find:

$$V(\psi) = \frac{V_{max} + V_{min}}{2} + \frac{V_{max} - V_{min}}{2} cos(\psi) \tag{3.28}$$

Deriving this equation one can obtain:

$$\frac{\partial V}{\partial \psi} = \frac{V_{max} - V_{min}}{2} (-sin(\psi)) \tag{3.29}$$

Putting oneself in the mid-fringe condition, it is possible to write the error on the voltage measurements as

$$\Delta V = \left| \frac{\partial V}{\partial \psi} \right|_{\frac{\pi}{2}} \Delta\psi \tag{3.30}$$

and from that, the relation for the error on the phase difference is determined:

$$\Delta\psi = \frac{2\Delta V}{V_{max} - V_{min}} \tag{3.31}$$

This result, expressed in Eq. 3.31, has been used to evaluate the sensitivity of the instrument in the configuration described in Par. 3.2.2.

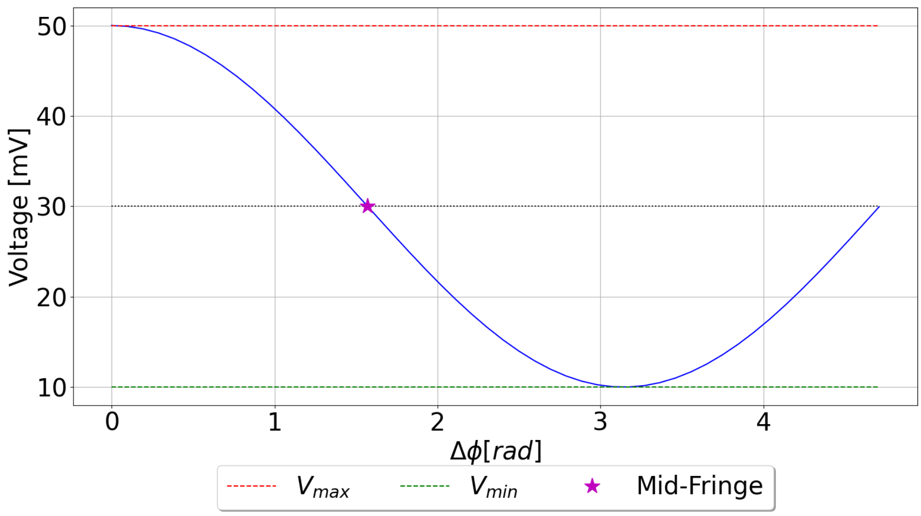

Figure 3.22: Voltage values collected by the photo-diode as a function of the optical path $\Delta\phi$.

The oscilloscope, connected to the photodiode output signal, was set so to collect different time ranges with a certain number of points collected per second, as shown in Tab. 3.9.
With the configuration explained in Par. 3.2.2, with the crystals at 45° with respect to the vertical polarization, the Quartz window was inserted between the two crystals, as explained in Fig. 3.10. Rotating the window, the interference pattern was detected.
The maximum and the minimum of the sinusoidal signal were measured, and their values were respectively $V_{max} = 62.8\ mV$ and $V_{min} = 32.0\ mV$. The working condition to collect the voltage values in the desired time range was, as explained before, the mid-fringe condition. In this case, the value of mid-fringe voltage is $V_{mf} = 47.4\ mV$. The window has been rotated until this condition of voltage was matched. Then the collection of the data was carried out.
Each of the time ranges has been collected multiple times so that it was possible to compare the different samples, deducing the statistical common behaviours.

Time Range	**Points collected**
1 s	10 k Pts
1 s	20 k Pts
100 s	1 M Pts

Table 3.9: Time range of collected data to estimate the sensitivity of the homodyne DI.

Starting from the time range of 1 s, the voltage has been collected two times. One of the sets is presented as an example in Fig. 3.23. The other set contains $10k$ *points*, while the other one $20k$ *points*.
Regarding the time range of 100 s, similar data have been collected. An exemplary graph of the data collected is shown in Fig. 3.24.

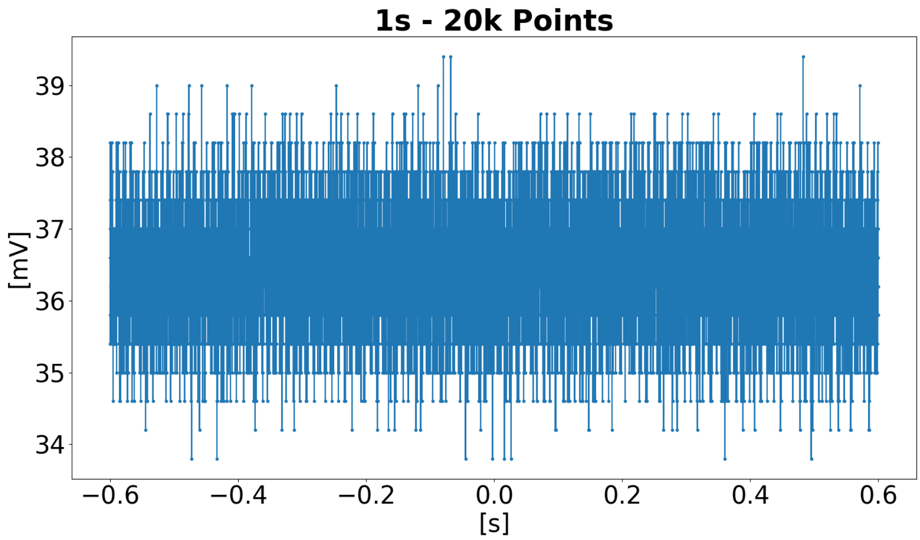

Figure 3.23: Voltage value collected at a fixed position of the Quartz window, which corresponds to the mid-fringe condition.

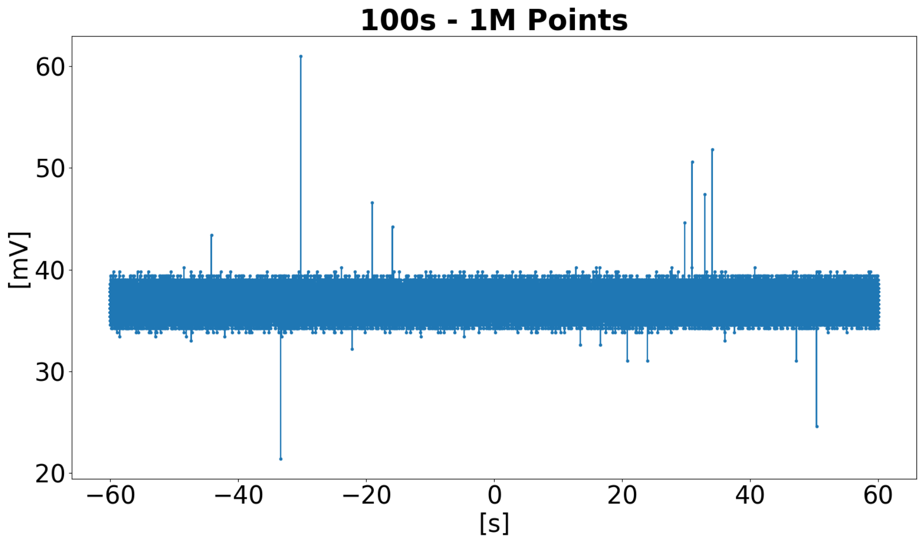

Figure 3.24: Voltage value collected at a fixed position of the Quartz window, which corresponds to the mid-fringe condition.

An estimate of the sensitivity of the instrument can be carried out relying on the presence of a drift in time for the voltage values collected.
The drift, in fact, determines the maximum sensitivity which is possible to obtain in the determination of the line integrated electron density analyzing the data from this instrument. Oscillations lower than this drift cannot be detected[18].

To analyze the data collected, they have been divided into samples containing 1000 points each. These samples are being averaged, and from each sample the mean value with the error associated with it will be calculated.
These sampled data are then plotted as a function of the timestep.
The drift in time of the voltage values was then detected fitting these plots with a linear function

$$V(T) = a + bT \tag{3.32}$$

where T is the time-step.

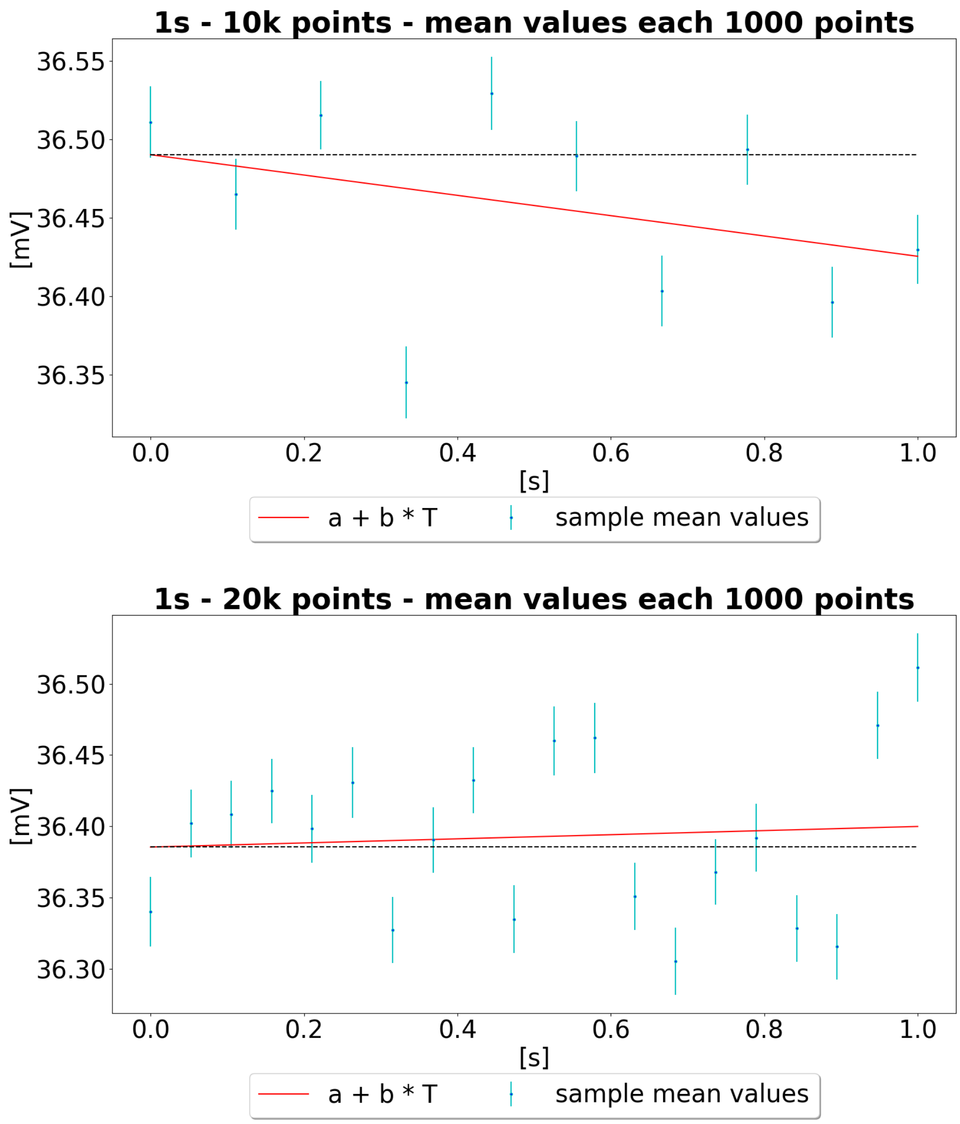

Figure 3.25: Mean values of voltages averaged every 1000 time-steps, for a data-set containing $10k$ points and one containing $20k$ points, shown with respect to the time; the data are fitted with a linear function, in order to determine the drift which the voltage undergoes during the time range of 1 s.

To obtain the right sampling, the data-set related to a time range of 1 s containing $10k$ *points* has been divided into 10 samples, while the one containing $20k$ *points* into 20.
On the other hand, for the time range of 100 s, which contains $1M$ *points*, the sample number chosen was 1000.
The resulting plots, accompanied by the fitted function, are shown in Fig. 3.25 and 3.26.
The results for the parameters of the fit are shown in Tab. 3.10.

Time Range	**Data-Set**	a	b
1 s	$10k$	36.49 mV	-0.0648 mV/s
1 s	$20k$	36.39 mV	0.0144 mV/s
100 s	1	36.67 mV	0.0020 mV/s
100 s	2	36.88 mV	0.0016 mV/s

Table 3.10: Results from the fitted linear function of the voltages sampled every 1000 timesteps.

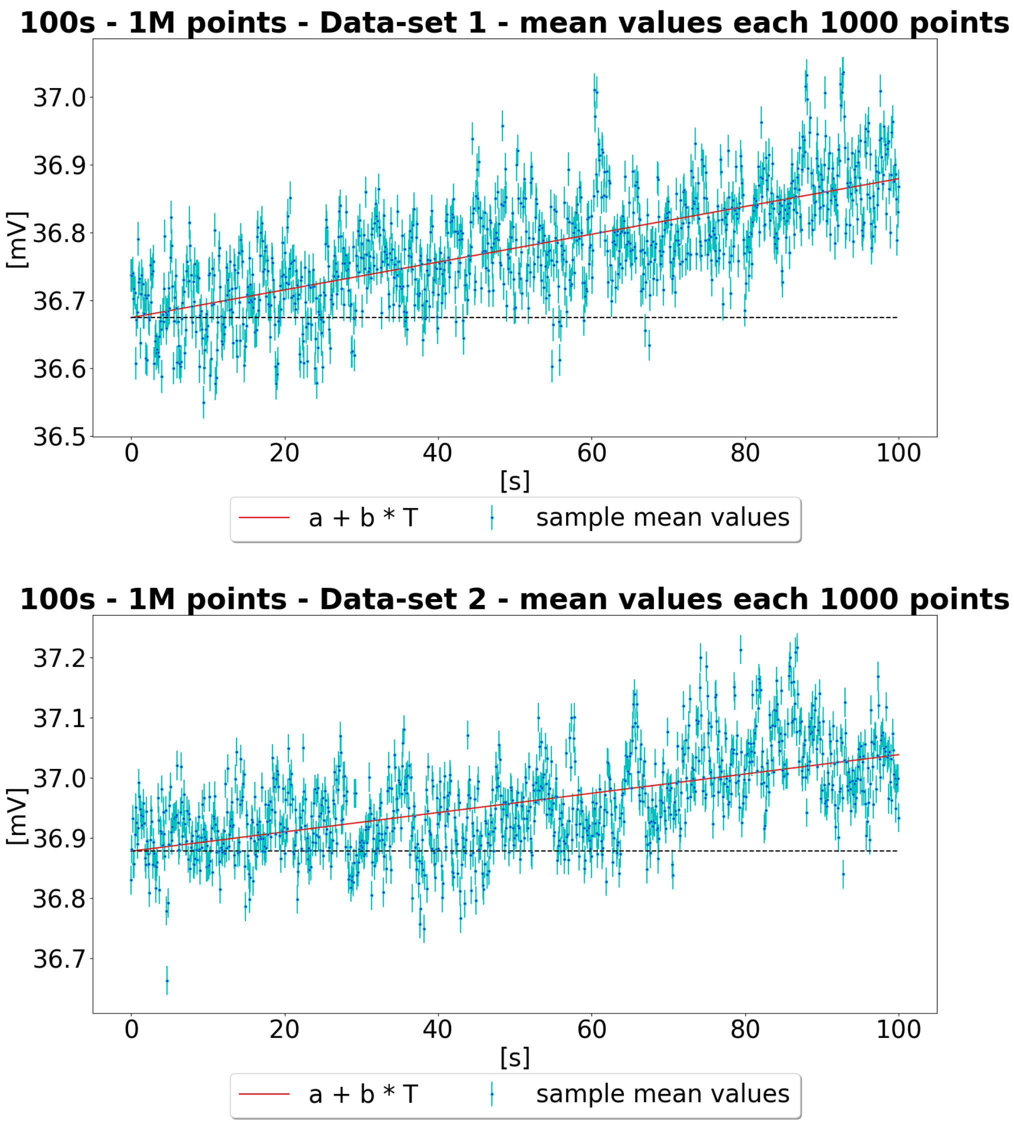

Figure 3.26: Mean values of voltages averaged every 1000 time-steps, shown with respect to the time, for the Data-set 1 and 2; the data are fitted with a linear function, in order to determine the drift which the voltage undergoes during the time range on 100 s.

We now assume that the value of the voltage drift in the time ranges considered can be chosen as the value associated with ΔV. From this value it is possible to compute the corresponding change in phase, $\Delta\psi$, as shown in Eq. 3.31.
From the change of phase, the sensitivity on the line integrated electron density is computed with Eq. 3.21.
The final results for the sensitivity are shown in Tab. 3.11.

Time Range	**Data-Set**	**Sensitivity for $\int n_e dl$**
1 s	10k	6.42 10^{17} m^{-2}
1 s	20k	1.43 10^{17} m^{-2}
100 s	1	2.03 10^{18} m^{-2}
100 s	2	1.59 10^{18} m^{-2}

Table 3.11: Results for the sensitivity of the line integrated electron density from the ΔV estimated by means of the time drift observed in a time range.

To conclude, the final estimate for the sensitivity for the line integrated electron density has been estimated for both the time ranges. The evaluation has been obtained by calculating the mean value between the sensitivity obtained in the two data-sets collected for both time ranges.
For the time range of 1 s, the sensitivity for $\int n_e \, dl$ is 3.925 10^{17} m^{-2}.
For the time range of 100 s, which is the characteristic time for the plasma duration in DTT, the sensitivity for $\int n_e \, dl$ is 1.81 10^{18} m^{-2}.

Dispersion interferometer at PROTO-SPHERA

PROTO-SPHERA (Spherical Plasma for Helicity Relaxation Assessment) is a new machine present at the laboratory of ENEA, Fusion and Nuclear Safety Department, Frascati.
Magnetically confined plasmas are usually formed inside toroidal vessels, where the plasma is surrounded by toroidal magnets. Some problems with this configuration are that the plasma-facing components and the conductors are, thus, subjected to severe thermal, nuclear and electromagnetichal loads in the region between the plasma and the axis of the toroidal structure.
In order to give proof of the feasibility to construct a magnetic confinement configuration able to overcome these problems, the PROTO-SPHERA project aims at producing hot toroidal plasma in a simply connected machine topology, i.e., without solid elements between the plasma and the axis[19],[20].

The toroidal magnetic field is generated by current flowing in the plasma around the axis (called the center post plasma discharge)[19].
An upgrade of PROTO-SPHERA is ongoing, in fact, the vacuum vessel and the structure has been completely renewed. A Dispersion Interferometer has been implemented as a diagnostic to measure the electron density for the machine. During the thesis work, I visited the experiment, working on some modifications and on the re-alignment phase. It was, then, given the chance to analyze some data, which had been collected when the machine was in function.

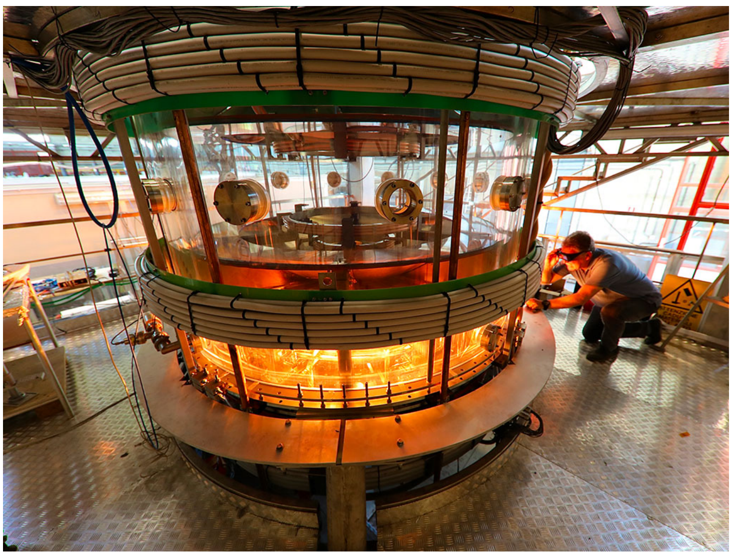

Figure 4.27: Picture of PROTO-SPHERA machine, at the laboratory of ENEA, Fusion and Nuclear Safety Department, Frascati.[21]

4.1 System Description

The DI mounted on PROTO-SPHERA is based on a continuous-wave Nd:YAG laser with wavelength $\lambda = 1064\ nm$. The scheme[22] of the instrument is shown in Fig. 4.28. It is a homodyne scheme, with some major differences with respect to the one built during our experiment.

The laser used for this instrument is a single-frequency monolithic laser, whose power can reach $1\ W$. To avoid back-reflection issues, an optical isolator is positioned as protection for the laser. The fundamental beam is collimated to a diameter of about $1\ mm$ with a focal length of $50\ cm$. The nonlinear crystals are type-I BIBO crystals, cut to work at $\lambda = 1064\ nm$. Their dimensions are $4\ mm \times 4\ mm \times 10\ mm$. The faces are coated to be anti-reflection for both the fundamental and the SH radiation.

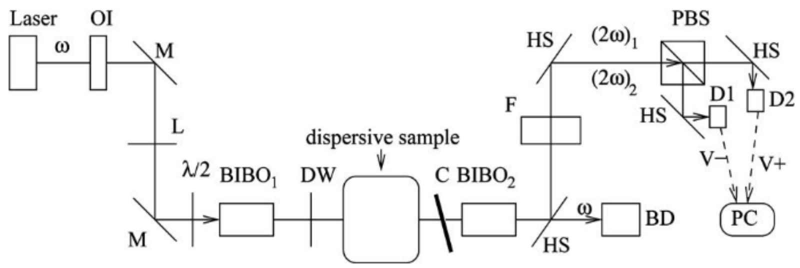

Figure 4.28: Scheme[22] of the DI mounted on PRTOTO-SPHERA machine, at the laboratory of ENEA, Fusion and Nuclear Safety Department, Frascati. OI stands for optical insulator, M for mirror, L for lens; $\lambda/2$ for the half-wave plate, BIBO for the nonlinear crystal, DW for the dual-wavelength wave plate, C for the compensator, HS is the harmonic separator, BD the beam dump, PBS the polarizing beam splitter, D1 and D2 are the light detectors, F a filter and V_+ and V_- the detector signals.

Following the scheme in Fig. 4.28, the polarization of the fundamental beam is rotated by a dual-wave plate (DW) in order to match the axis of the nonlinear crystals.
The two BIBO crystals are both set with parallel orientations. In order to overcome the problem related to the two SH beams having the same polarization, a dual wavelength plate, acting as a half-wave for the SH beam with wavelength $\lambda = 532\ nm$, and as a full-wave for the fundamental one ($\lambda = 1064\ nm$), is used.
It rotates of 90° the SH beam generated by the first crystal while leaving unaffected the polarization of the fundamental beam.

In the system, then, there is a compensator, made of a tilted BK7 window, of thickness $6\ mm$, with anti-reflection coating for both wavelengths. Thanks to the presence of this window, it is possible to compensate very well spurious dispersion signals which may be acquired travelling through the optical elements.

After the second crystal, a filter F removes the fundamental beam. At last, a polarizer beam-splitter (PBS) is set in the path of the two SH beams, generated by the two crystals. This beam-splitter is set so that to transmit at 45° with respect to the polarization of the SH beams. The reason for including the beam-splitter is that, with this configuration, there are two signals, the transmitted and reflected one, which show a complementary interference pattern (they have a phase difference equal to π).
The signal is then collected by two Si-PIN photodiodes (D1 and D2), which transmit the signals to two low-noise variable gain amplifiers.

Denoting the two recorded signals V_+ and V_-, they are combined as

$$R = \frac{V_+ - V_-}{V_+ + V_-} \tag{4.33}$$

From the computed signal R it is possible to deduce the information about the phase difference.

This system is a homodyne interferometer since the interference is between the two SH beams. This configuration is characterized by a simple system, being the two beams always superimposed. Its peculiar detection, which is based on two signals with a fixed phase difference of π, offers a very good sensitivity[22].

4.2 Realignment and Changes in the Optics

During the visit to ENEA laboratories, the machine PROTO-SPHERA was not actively working with plasma production. The interferometer needed to be re-aligned.
The DI mounted on PROTO-SPHERA follows the scheme described in the previous paragraph. After the first SH beam is generated, this beam and the fundamental one pass through the plasma alongside its diameter.

Figure 4.29: Picture of the second half of the DI on PROTO-SPHERA, mounted on the machine.

The first half of the interferometer, defined as the part of the interferometer before the plasma, has been left untouched.
The second half, mounted on a hanging structure (Fig. 4.29), was originally composed as explained in Fig. 4.30, where W is the wedge used as compensation, L is one lens (focal length equal to 250 mm) to focus the beam inside the crystal, $C2$ is the second crystal, F is a filter which eliminates the fundamental beam, and BS is the beam-splitter.
The focus was made using a single lens with a focal length of 250 mm, and it was positioned around 27 cm before the position of the crystal.

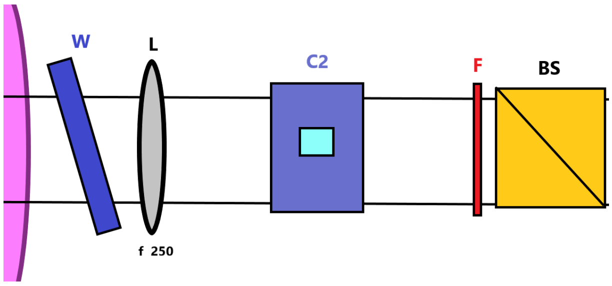

Figure 4.30: Original scheme of the second half of the DI mounted on PROTO-SPHERA. W stands for window, L for the lens, C2 is the second crystal, F the filter and BS the beam splitter.

The signal achieved with this configuration was not great, with V_+ with a value of about 20 mV, and V_- of about 30 mV. We decided to slightly change the configuration, modifying the focus. The new configuration is shown in Fig. 4.31. The main alteration is that now two different lenses were used, $L1$ with a focal length of 80 mm and $L2$ with a focal length pf 60 mm. They are positioned respectively before and after the crystal, such that they are 140 mm away from each other, and the crystal is positioned 80 mm after $L1$, at its focus.

The system was then optimized. The signals at the end of the optimization were $V_+ \simeq 0.7$ V and $V_- \simeq 0.15$ V.
Since the plasma was not produced, being the machine not in function, some test measurements have been done using a flame. The signal did detect the "plasma", showing in the two signals a peak in opposition of phase.

Some of the difficulties encountered during the alignment were related to the hanging structure which holds the system after the passage inside the plasma, and the compensation plate. All the optics are hung on a linear structure (Fig. 4.29), so there are not many degrees of freedom. In addition, the structure is not stable enough, and the alignment is lost easily. For these reasons, the alignment is quite time-consuming.
In the future, a different hanging system will be developed, using a portion of optical bench. It will be rotated of 90° with respect to the present configuration, so as not to be at risk of mechanical hits. Mirrors will be introduced in order to deflect the beam inside the crystals, giving more freedom in the alignment.
About the compensation plate, it is now hung on a holder which is not graduated, and so its movements are manually operated. The precision in the positioning phase is not as high as in the system described in [22], and for this reason, the sensitivity reachable with this instrument is worse than the one of the prototype described.

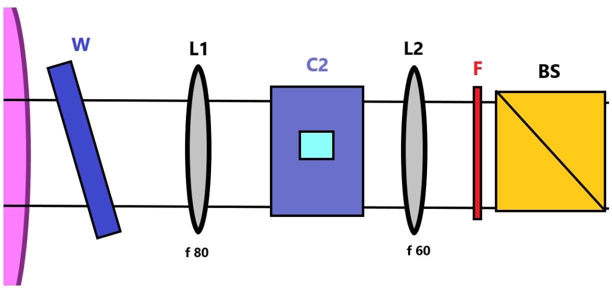

Figure 4.31: Modified scheme of the second half of the DI mounted on PROTO-SPHERA. W stands for window, L1 and L2 for the lenses, C2 is the second crystal, F the filter and BS the beam splitter.

4.3 Data Analysis

A Data-set was collected when the PROTO-SPHERA machine was in operation, producing plasma. I proceeded with its analysis, trying to deduct the density value from it.

The raw data presented time values, V_+ and V_-. The values have been filtered using a low pass digital filter implemented on a python routine. From them, the value of R as defined in Eq. 4.33 is calculated. The resulting value is shown in Fig. 4.32. In Fig. 4.33 and 4.34 also the voltage values are shown.

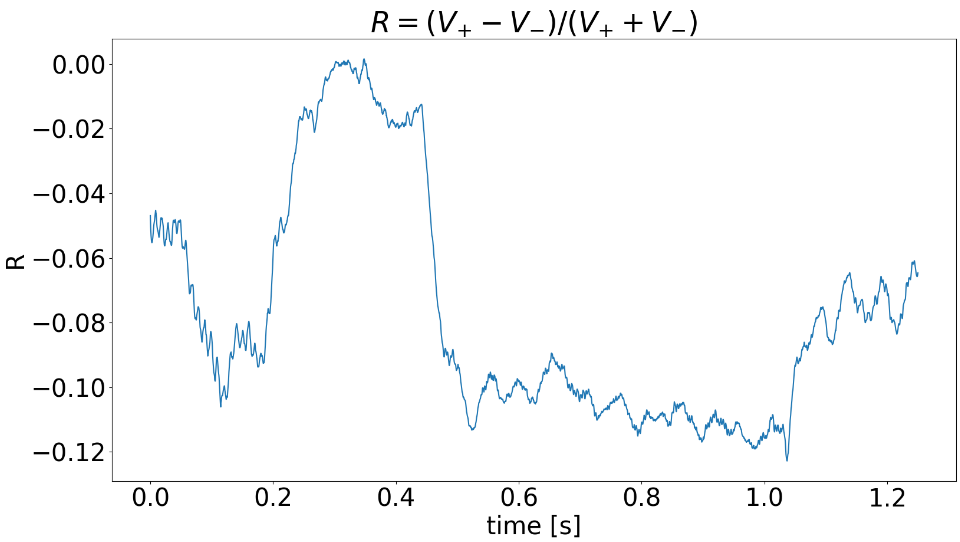

Figure 4.32: Analysis from the DI on PROTO-SPHERA. Values of R (Eq. 4.33) as a function of time.

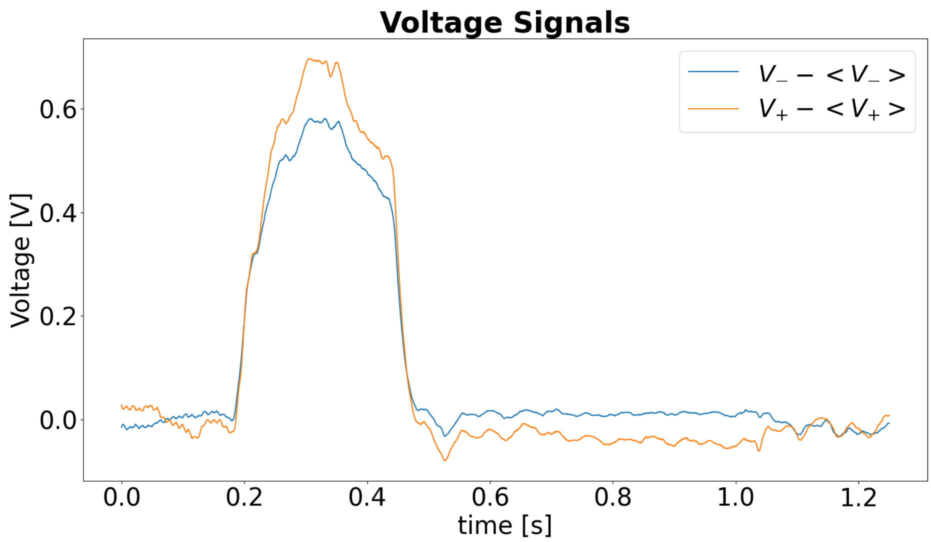

Figure 4.33: Analysis from the DI on PROTO-SPHERA. Values of the voltages V_+ and V_- as a function of time.

To obtain the line density value Eq. 1.18 and 3.20 have been inverted. The length of the path inside the plasma was necessary. Its value is equal to 0.6 m. To obtain the right value of density, the background has been subtracted. The line density behaviour can be observed in Fig. 4.35, where the line density value, with the background subtracted, is plotted as a function of time. An estimate of the average plasma line electron density is obtained by evaluating the mean value of the peak visible in Fig. 4.35 has been calculated. The obtained result is

$$n_e = 2.921\ 10^{19} m^{-3} \tag{4.34}$$

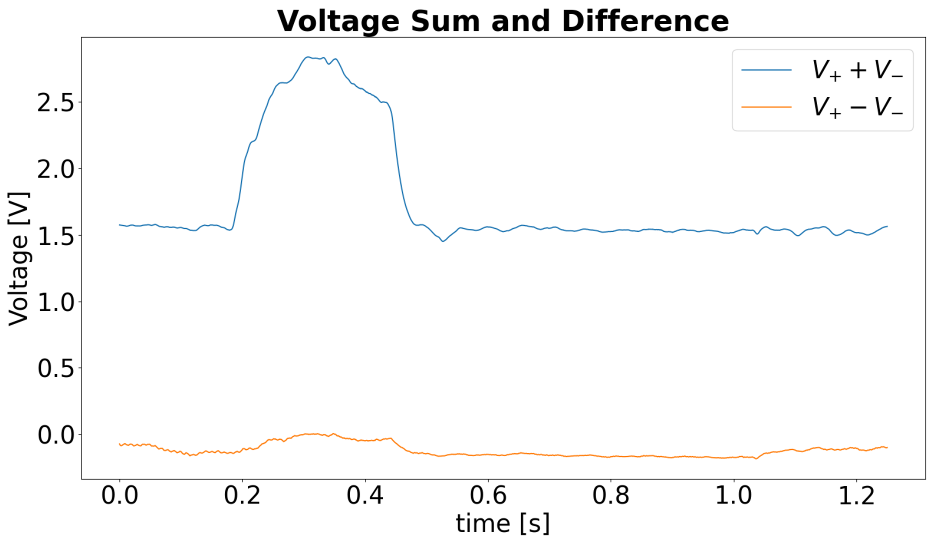

Figure 4.34: Analysis from the DI on PROTO-SPHERA. Values of the sum and difference of the voltages V_+ and V_- as a function of time.

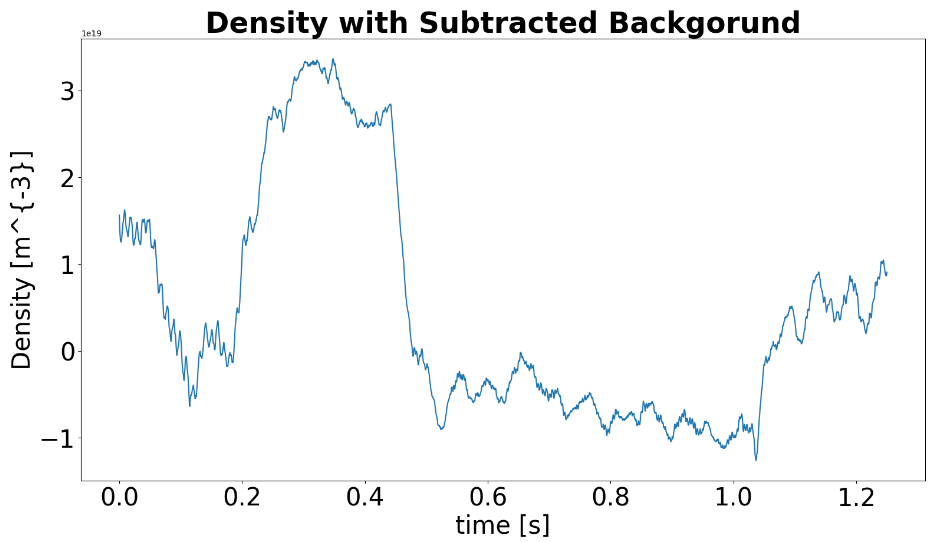

Figure 4.35: Analysis from the DI on PROTO-SPHERA. Values of the line electron density re-normalized in order to subtract the background, as a function of time.

Heterodyne Configuration

5.1 Schematic Description and Experimental Realization

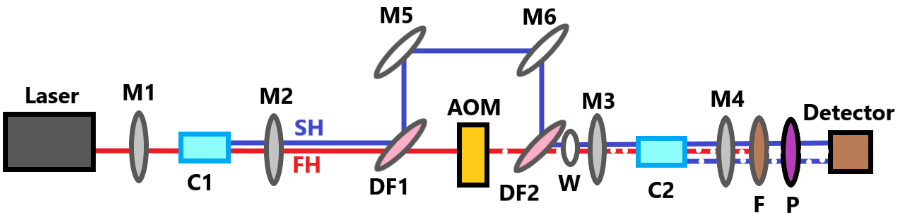

Figure 5.36: Heterodyne interferometer scheme. To the left you can find the laser source; M1, M2, M3 and M4 are concave mirrors, C1 is the first LBO crystal, C2 is the second one, DF1 and DF2 are dichroic mirrors which transmit the fundamental beam while reflecting the SH beam, M5 and M6 are plane mirrors, W is the window that simulates the plasma, F is a filter that blocks the FH beam, P is a polarized and to the right the detector is shown.

A problem that arises with a DI homodyne scheme is that with this configuration the phase measurement depends on the intensity of the signal detected. Therefore if the laser power emission changes or the gain of the detection system changes there will be errors in the phase measurements[23].

A different approach that can be explored is a phase modulation method, based on a heterodyne configuration.
The heterodyne scheme studied during this thesis work is shown in Fig. 5.36. A phase modulation is added to the FH beam with an Acousto Optic Modulator (AOM). The modulation is added to the FH beam before it passes through the second crystal, and this translates into a known modulation of the SH beam generated inside the second crystal. The fundamental frequency shifted and the SH one generated by the first crystal pass through a window (W) which introduces a phase difference with respect to the incidence angle. Then the modulated FH beam passes through the crystal, generating another SH beam. The interference signal between the two SH beams is thus detected.
The detection system exploits the demodulation of the interference signal using as a reference the alternate signal driven by a radio-frequency driver that powers the AOM.

The interference signal for a heterodyne system can be described by the equation[15]

$$\overline{E^2} = ... \ + (E_1 \ E_2 \ cos(\Delta\phi))\, cos(\Delta\omega t) + (E_1 \ E_2 \ sin(\Delta\phi))\, sin(\Delta\omega t) \qquad (5.35)$$

The line density information is contained in the coefficients of the signals in phase and quadrature. By demodulating the detected signal it is possible to obtain an estimate of the phase difference $\Delta\phi$ which is independent of the intensity of the laser.

A complication of this setup is the necessity to separate the two beams, the SH and the FH. In order to introduce a modulation only in the FH beam. For this reason, their paths are not always superimposed as before. In addition, there are some optical elements that are not shared by both of them: for example the mirrors $M5$ and $M6$ in Fig. 5.36. If they are subject to vibrations, they can add a vibrational component to the phase of the SH beam, which will affect the interferometric signal.

This setup has been designed and studied, and it will be built in the following months.
To build this configuration on the optical bench, the main part of the setup from the homodyne DI will be kept. The biggest challenge will be the alignment of the SH beam deviated, given the difficulty to detect the beam at 0.775 μm.
Another important element that is new to the setup is the AOM. It is necessary to know its effect on the beams. In the next paragraphs its behaviour will be described and then tested.

5.2 AOM Description and Operation

The AOM, also called "Bragg cell", is an optical element used to diffract and shift the frequency of a laser beam. Its functioning is based on the *acousto-optic effect*: the refractive index of some crystals is modified by the mechanical strain of a sound wave.
In the specific case, the material is AMTIR, as shown in Appendix A, Fig. 7.50 and 7.51.
The sound wave generates moving periodic wave-fronts, compressing and expanding the lattice. These wave-fronts are responsible for periodic maxima and minima of the refractive index.
The incoming laser beam is thus scattered with respect to these periodic refractive indices. A pattern of diffraction is created. Since the travelling acoustic waves cause a motion of the crystal planes, due to the Doppler effect the deflected beams are also shifted in frequency.

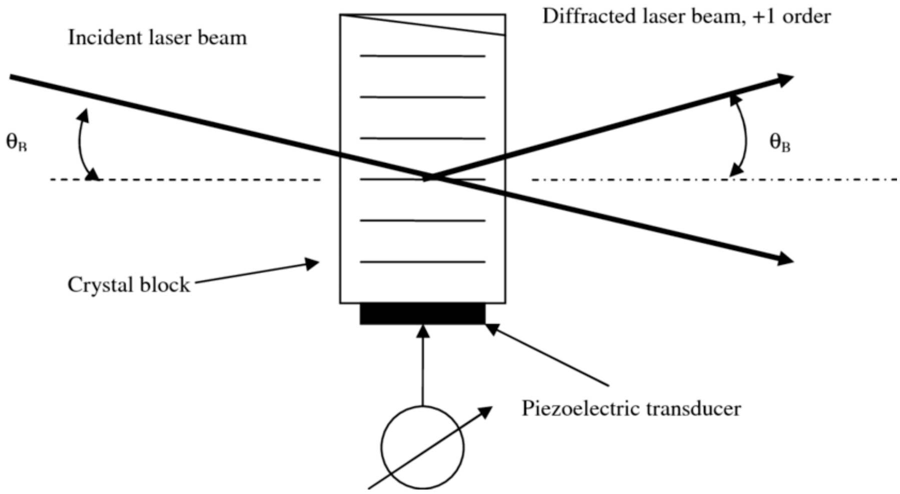

Figure 5.37: Scheme of the first order diffraction of an AOM[24]

The scattering pattern is the Bragg diffraction one.
Given a radiation characterized by a certain wavelength λ, and the angle between the laser beam propagation direction and the AOM optical axis θ, the diffraction pattern is characterized by the equation[25]

$$m\ \lambda = 2\ d\ sin\theta \tag{5.36}$$

where m is an integer and d is the grating constant of the crystal.

The diffraction is characterized by the *Bragg condition*, which fixes the value of the incident angle θ as[26]

$$\theta_B \simeq sin\theta_B = \frac{\lambda}{2\ n\ \Lambda} \tag{5.37}$$

where θ_B is the Bragg angle, n is the refractive index, and Λ is the wavelength of the sound wave injected in the crystal.

The deflected beam undergoes a frequency shift due to the fact that the crystal planes move with a certain velocity v_s (the velocity of the acoustic waves): for the Doppler effect the deflected beam is characterized by the frequency

$$\omega_d = \omega \pm \frac{2\pi}{\Lambda} v_s \tag{5.38}$$

For the first order of diffraction, the input and the output angles are equal to θ_B. This condition is shown in Fig. 5.37.
In general, the m-th order of diffraction is given by[26]

$$2\ \Lambda\ sin\theta = m\frac{\lambda}{n} \tag{5.39}$$

The amount of light diffracted depends on the intensity of the sound wave injected.

For the specific case of the AOM used for this setup, the Bragg angle for the fundamental beam is equal to 12 $mrad$ and was given by the characteristics of the instrument (Appendix A, Fig. 7.50 and 7.51).
It was then evaluated also the Bragg angle for the SH, inverting the relation just explained. The resulting value for $m = 1$ is 6 $mrad$.

5.3 AOM Installation and Test

Figure 5.38: AOM set on the optical bench.

During the preparation phase of the Heterodyne configuration, the AOM has been inserted into the optical system on the optical bench.
The first test intended to ensure the working condition of the AOM on the fundamental beam ($\lambda = 1.55\ \mu m$) and the possible effects on the SH and the SHG on the second crystal.
The system was the same as the one used in the Homodyne configuration, with both of the crystals generating a SH beam, as in Par. 3.2.2.

The AOM was inserted on the optical bench, between the two pairs of concave mirrors, in the same position as the Quartz window in the Homodyne configuration (Fig. 5.38). The AOM was oriented in order to observe the diffracted 0^{th} and 1^{st} orders of the fundamental beam. The RF driver could be used in different conditions, based on the use of a power supply able to select the RF power or working in minimal power conditions (without the external power supply).

It was seen that, with the RF driver switched off, the beam was not undergoing an appreciable diffraction, while using the RF driver the 1^{st} order diffracted beam was seen. For higher values of the power of the RF driver the power of the 1^{st} order diffracted beam was higher than the 0^{th} order.

The value chosen for the working condition for this test is 0.3 V. For lower values of power (0.1 V) the diffraction was not observed, and for higher values (0.5 V) the power converted in 1^{st} order diffracted beam was higher than the 0^{th} order, so not enough fundamental beam was able to reach the second crystal to generate SH.
Positioning a filter that blocks the fundamental beam before the second crystal, only the SH generated in the first crystal was observed.
Using instead a filter that blocks the SH beam, and positioning it right after the first crystal, only the signal from the second crystal was selected.

The signal of the SH beam generated in the first crystal was not detected, neither with the RF driver switched off, nor with the Bragg cell actively diffracting.
However, the SH beam from the second crystal, generated by the fundamental 0^{th} order passing unchanged by the AOM, was detected, positioning the filter which blocks the SH beam before the second crystal. The detected signals, with the RF driver switched on and off, are shown in Tab. 5.12.

The total signal has also been collected, recording the voltage values without any filter present in the beams path. These values are shown in Tab. 5.12 too.

RF driver	**Filter**	**Voltage**
OFF	1.55 μm filter	$V_2 = 6.6\ mV$
ON	1.55 μm filter	$V_2 = 5\ mV$
OFF	No filter	$V_{tot} = 12\ mV$
ON	No filter	$V_{tot} = 8.4\ mV$

Table 5.12: Voltage values for the signal of SH beam generated by the second crystal, with and without the effect of the AOM. V_{tot} is the total signal collected, without the presence of filters; V_2 is the signal of the SH beam generated by the second crystal, obtained by positioning a filter that blocks the SH after the first crystal and before the second one.

From these values, it is possible to infer that the effect of the AOM changes the power value of the 0^{th} order, reducing it, and causing also a reduction in the SH power generated by this 0^{th} order beam when travelling through the second crystal. The total value of the voltages, V_{tot}, which represents the interference of both the SH beams, from the first and the second crystal, is higher than only the second crystal SH beam voltage. This is a confirmation that there is, in fact, some part of SH signal coming from the first crystal. To be sure of that, the Quartz window has been inserted after the AOM, and its orientation has been rotated. An interferometric pattern has been observed: this is a confirmation of the fact that both of the SH beams are present.
The reason why the SH beam from the first crystal is not detected might be that its power is very low. The noise collected during these measurements was around 2.64 mV, so if the SH beam from the first crystal has a lower voltage value (which is compatible with the results obtained for the interference) the signal cannot be detected.

The question which arises is why the signal voltage of the SH beam generated in the first crystal is so low when the AOM is inserted in the optical path. This voltage, in fact, has not been recorded neither with the AOM switched on, nor with it switched off. Some of the possible reasons for this are related to the material of the cell:

- There is a deviation of the SH beam that in part misses the detector;
- The material of the cell has a high absorption of the SH beam;
- The cell has a reflecting coating which causes the SH beam to be reflected while the fundamental beam is let through;
- The diffractive beam at the order $m = 2$ for the SH beam may be generated: it corresponds to the diffractive condition for the wavelength of the SH beam ($0.775\ \mu m$) at the input angle equal to 12 $mrad$.

To eliminate the possibility of a deviation, the detector has been moved in the vertical and in the horizontal direction, in order to see if moving it the whole SH beam from the first crystal was collected. Since an interferometric signal was indeed collected, the SH from the first crystal could not be much deviated, since some part of it, at least, arrived at the detector. There was no improvement, so the hypothesis of a deviation was ruled out.
As presented in Appendix A Fig. 7.50 and 7.51, the material of the AO frequency shifter is AMTIR. The absorption coefficient for wavelength 0.775 μm is $\alpha = 0.095025 cm^{-1}$. Since the dimensions of the cell are 25 mm, the total absorption of the SH is about 38.01%. The nominal absorption for the fundamental beam is much lower, around 5%. Thus, the absorption of the SH is considerable, and cannot be neglected.
The presence of a reflecting coating was indicated by the supplier: the nominal transmittance for the fundamental beam is 95%, but they were not able to give an estimate of the reflectivity for the SH beam wavelength 0.775 μm.
To conclude, the material of the AOM is not optimal to work with this wavelength.
It was not possible to exclude the possibility of the diffraction at the order $m = 2$ of the SH beam because the experimental setup did not give the possibility to have an easy detection of the SH, given its low intensity.

Further analysis will be needed in the future, to establish if a significant amount of the SH beam power is deviated by the AOM to the $m = 2$ diffraction order, modulating it.
This is an important issue, in particular for the theoretical study which will follow in the next chapter. The idea is to design a system where, with the aid of a prism, both of the beams, the fundamental and the SH one, can enter the AOM with such angles that only the fundamental beam is modulated. This system may resolve the problem of the non superimposition of the beams, present in the heterodyne configuration.
For this system to work the AOM must not affect the SH beam.

Superposition of different beams by means of prism optics

As explained in the previous paragraph, one of the issues related to the previous heterodyne configuration is the fact that the superposition of the two beams which form the DI is not ensured along all their paths.

To overcome this problem, a different scheme was introduced: if the beams were let pass through a prism, or a prism system, which changes their angles so that they are compatible with the AOM operation, it could be possible to reduce the non-superimposition to a minimum.
Some theoretical studies have been carried out, which explore different possible configurations. They were all based on the instrumentation available in the laboratory since the idea is to try and implement them on our setup. The AOM supplied is suitable for the fundamental beam, so the schemes developed are all based on the modulation of the FH beam.
The problem related to the available AOM is that, as was found in the tests explained in Par. 5.3, the SH beam passing through it presents an important loss in power, which may be caused by the diffraction of this beam to its order $m = 2$ and by the absorption in the AOM material, since we can see the power loss both with the AOM turned on and with the AOM turned off
An alternative system, with an AOM which modulates the SH, may open different possibilities.

6.1 Single-Prism Solution

The simplest scheme would require to use only one prism.
The system requires that the two beams, the SH and the FH, arrive superimposed at the first face of the prism. The effect that the prism should apply to the beams is to change their trajectory so that the fundamental one arrives at the AOM with an angle of 12 $mrad$, which is equal to the value of the Bragg angle for that frequency, while the SH beam should be deviated of -12 $mrad$. The reason for this choice is that the fundamental beam will be diffracted, and the modulated beam at the first order of diffraction will exit the AOM with an angle of -12 $mrad$, and so exiting the AOM the two beams are superimposed.
This simple and clean description, however, cannot be achieved, due to the refractive indices of the two beams.
The evaluation of the deflection of the two beams has been carried out, considering a prism made of K7 or SF5 optical glasses.
Their indices of refraction have been evaluated using the *Sellmeier Formula*[27]

$$n(\lambda) = \sqrt{1 + \sum_j \frac{B_j \lambda^2}{\lambda^2 - C_j^2}} \tag{6.40}$$

which gives the refractive index of a transparent optical material as a function of the wavelength.
The coefficients were found in literature.

The resulting indices are shown in Tab. 6.13.

Material	$n_{1.55}$	$n_{0.775}$
K7	1.4954	1.5054
SF5	1.6422	1.6597

Table 6.13: Refractive indices for two different materials, at the wavelength of the fundamental and SH beam.

Computing the deflection of the fundamental and the SH beam, impinging with the same trajectory, shows that, for a prism with a generic convex dihedral angle A, the fundamental beam is deviated less than the SH beam (Fig. 6.39).
Given the input angle θ_{i1}, equal for both the beams, the output angles exiting the prism will be given by

$$\theta_{t2} = arcsin\left(sin\left[A - arcsin\left(\frac{sin\theta_{i1}}{n}\right)\right] n\right) \tag{6.41}$$

where, for the fundamental beam the $n = n_{1.55}$, while for the SH beam $n = n_{0.775}$.
Form Fig. 6.39 it is possible to see that the beams will diverge, and so it is not possible to achieve a configuration where the exiting angle for the fundamental beam is equal to 12 $mrad$, while the one for the SH beam is -12 $mrad$, as desired.

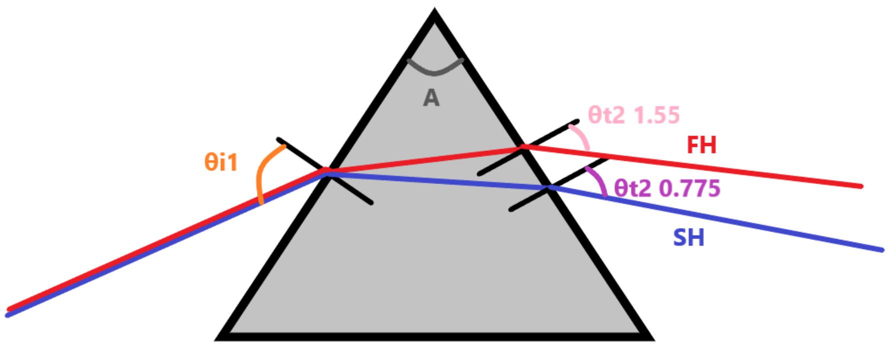

Figure 6.39: Scheme of the deflected beams in a generic prism. FH is the fundamental beam, while SH defines the second harmonic beam.

A different approach was then applied. The idea is to have exiting beams such that the fundamental beam arrives at the AOM at the Bragg angle. Arriving there with this configuration, the beams which will exit the AOM (first diffracted order beam) will travel with a trajectory with an angle of -12 $mrad$ with respect to the normal of the AOM. The condition imposed is for the two beams to be parallel after the AOM. The beams will be needed to travel close enough that, given their waist, there will be an interaction in order to create an interferometric signal.
For this system, the K7 glass is chosen as the material for the prism.
This system is shown in Fig. 6.40.

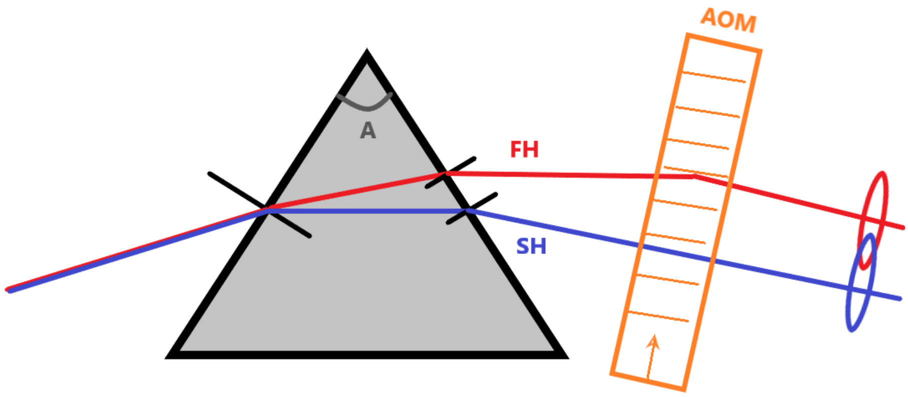

Figure 6.40: Scheme of the configuration with one prism. The fundamental beam is called FH, while the second harmonic SH. On the right, it is possible to see the schematic description of the beams waist, to give an idea of the partial superposition after the fundamental beam is deviated, and modulated, by the AOM.

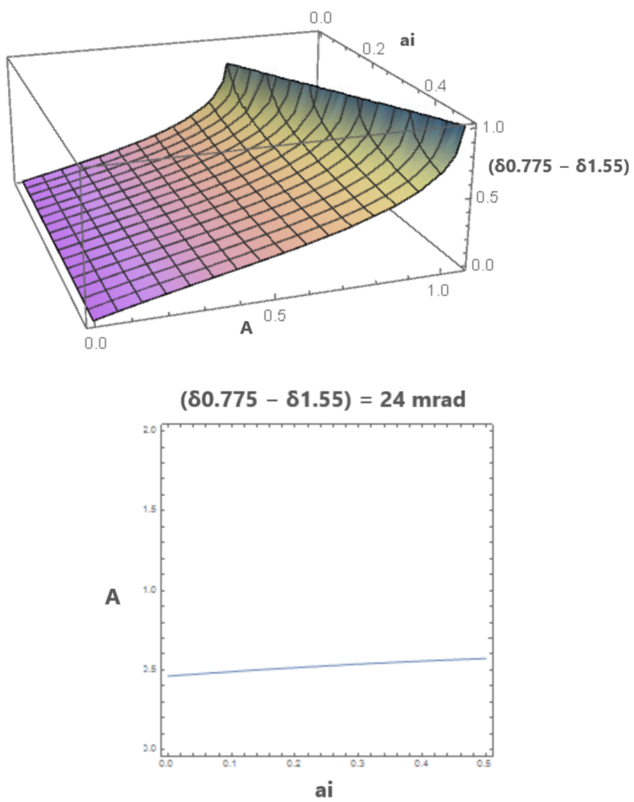

Figure 6.41: (up) Plot of the equation $(\delta_{0.775} - \delta_{1.55})$ with respect to the input angle θ_{i1} and the prism angle A; (down) Plot of the contour of the equation $(\delta_{0.775} - \delta_{1.55})$ for the fixed value 24 $mrad$. On the horizontal axis there is the input angle θ_{i1} and on the vertical axis the prism angle A.

The condition imposed is that the difference of the deviation angles (plotted in Fig. 6.41), defined as $\delta = \theta_{t2} - \theta_{i1}$, for the fundamental and second harmonic beams is 24 $mrad$.
Positioning the AOM in order to have the fundamental beam arriving at the modulator with an angle equal to the Bragg (12 $mrad$), the modulated fundamental beam will exit the AOM with an angle equal to -12 $mrad$.
The condition just defined ensures that, with this configuration, the SH beam travels with a trajectory which lays at an angle equal to -12 $mrad$ with the optical axis of the AOM, and thus will be almost parallel to the modulated fundamental beam.

The computation has been carried out with a Wolfram Mathematica routine, which plotted the contour of solutions with these conditions (Fig. 6.41). Then the values of the input angle $\theta_i 1$, and the value of the angle A of the prism have been evaluated so as to obtain:

$$\delta_{0.775} - \delta_{1.55} = 24 \; mrad \qquad (6.42)$$

The values are shown in Tab. 6.14.

The requirement for the interference of the fundamental beam with the SH one is that their waists superimpose. Given an average waist value of 1.4 mm, the minimum requested distance between the two centers of the beams is 0.7 mm. This way we can obtain at least a 50% superposition. Such a distance translates into a distance between the prism and the AOM equal to

$$L \simeq \frac{0.7\ mm}{24\ mrad} = 29\ mm \tag{6.43}$$

These values are compatible with a working system. This solution is, thus, feasible.

Material	$(\delta_{0.775} - \delta_{1.55})$	θ_{i1}	A
K7	24 $mrad$	0.15 rad	0.237 rad

Table 6.14: Values of the input angle θ_{i1} and the prism angle A so that the condition 6.42 is fulfilled.

6.2 Double-Prism Solution

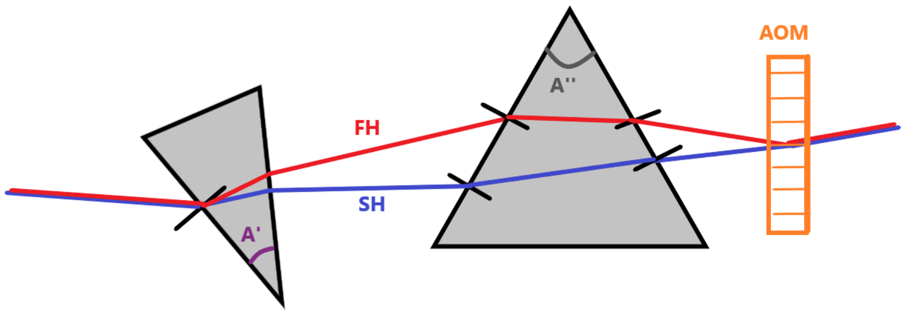

Figure 6.42: Scheme of the configuration with two prisms. The fundamental beam is called FH, while the second harmonic SH.

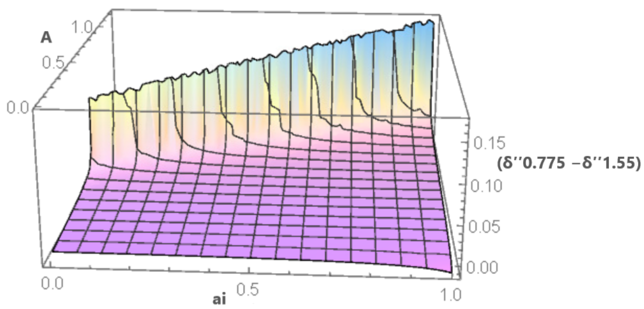

Figure 6.43: Plot of the equation $(\delta_{0.775} - \delta_{1.55})$ with respect to the input angle $\theta_{i1}^{''}$ and the prism angle $A^{''}$ for the second prism.

An alternative solution to optimize the superimposition of the fundamental and SH beam can be designed with two prisms.
Exploiting different refractive indices using two different materials for the two prisms, it is possible to build a system as the one shown in Fig. 6.42.
The combination of the deviation of the two prisms gives an angle difference between the exit angle of the fundamental and of the SH beam of 24 $mrad$, so that they superimpose after the AOM effect on the fundamental beam.

The first prism is chosen to be made of K7, as the one treated in the previous paragraph, while the material of the second prism is SF5. Their indices of refraction are shown in Tab. 6.13.
The first chosen condition, imposed for the first prism, is that the difference in the deviation angles of the fundamental and SH beam is set:

$$\delta_{0.775}^{'} - \delta_{1.55}^{'} = 6\ mrad \tag{6.44}$$

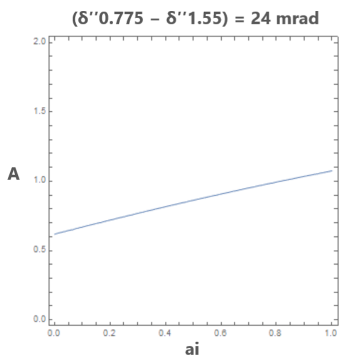

Figure 6.44: Plot of the contour of the equation $(\delta^{''}_{0.775} - \delta^{''}_{1.55})$ for the fixed value 24 $mrad$. On the horizontal axis, there is the input angle $\theta^{''}_{i1}$ and on the vertical axis the prism angle $A^{''}$.

To obtain the values of the input angle θ_{i1} and the prism angle A', an analogous method to the one explain in the previous paragraph has been carried out.
This choice was dictated by the desire of having a small angle, so that the realization of the second prism will be easier. In fact, we will see that with a larger difference in the deviation angle the distance between the first prism and the second becomes too large.

The condition for the input angles at the second prism, which now do not coincide, is that, being the input angle for the fundamental beam $\theta^{1.55}_{i1} = \theta^{''}_{i1}$, the input angle for the SH beam will be $\theta^{0.775}_{i1'} = \theta^{''}_{i1} + 6\ mrad$.
With this condition, the equation of the difference of the deviation angles is obtained.
The new requirement is that, with these input angles, the deviation caused by the second prism is such that

$$\delta^{''}_{0.775} - \delta^{''}_{1.55} = 24\ mrad \tag{6.45}$$

The computation has been carried out again with a Wolfram Mathematica routine, which plotted the contour of solutions with these conditions (Fig. 6.43 and 6.44). Then the values of the input angle $\theta_i 1$, and the value of the angle A of the prism have been evaluated so to obtain the relation 6.45. They are shown in Tab. 6.15

Material	$(\delta_{0.775} - \delta_{1.55})$	θ_{i1}	A
K7	6 $mrad$	0.7827 rad	0.5983 rad
SF5	24 $mrad$	0.49445 rad	0.863 rad

Table 6.15: Values of the input angle θ_{i1} and the prism angle $A^{'}$ for the first prism so that the condition 6.44 is fulfilled and values of the input angle $\theta^{''}_{i1}$ and the prism angle $A^{''}$ for the second prism so that the condition 6.45 is fulfilled

Defining the distance between the first prism and the second prism with L, and the distance between the second crystal and the AOM as L', with some approximations, it is possible to write the relation

$$L\ \beta = L'\ \alpha \tag{6.46}$$

being $\beta = \delta^{'}_{0.775} - \delta^{'}_{1.55} = 6\ mrad$ and $\alpha = \delta^{''}_{0.775} - \delta^{''}_{1.55} = 24\ mrad$. Their definition is also shown in Fig. 6.45.
To determine the feasibility of this configuration, we need to estimate the values of L and L'.
In the previous paragraph, we set a beam separation at a distance L equal to 0.7 mm, since we needed the superposition of the beams. In this configuration, however, there is no need for such a request.
The assumption made in this case is to have a distance between the second prism and the AOM equal to 3 cm.
With this assumption on the value of L', using the relation 6.46, the corresponding value of L is

$$L = \frac{L'\ \alpha}{\beta} = 12\ cm \tag{6.47}$$

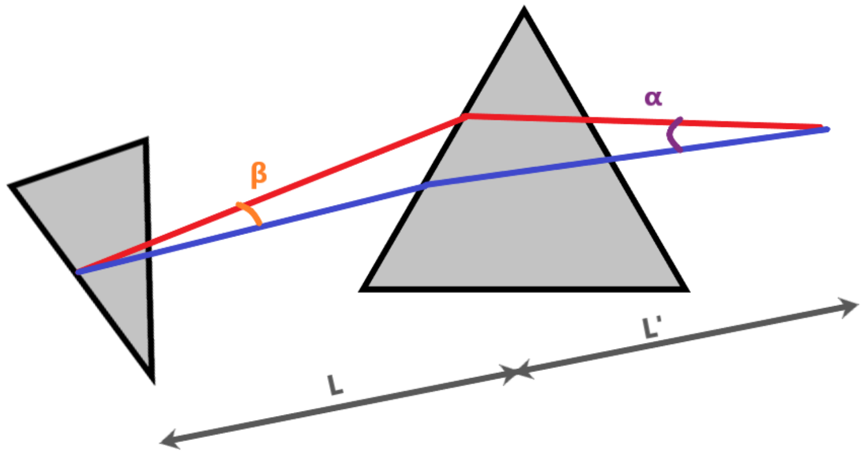

Figure 6.45: Scheme of the configuration with two prisms, focusing on the distance values between the two prisms and between the second prism and the AOM.

This last configuration, where two prisms are used to deflect the SH and the FH beams in order to achieve the desired angle to modulate the latter is considered the most promising.

Conclusions

This work aimed to start the study, design and development of a dispersion interferometer for DTT. This type of instrument is quite an innovative diagnostic for the electron density in large plasma machines, and is a very promising solution. It offers good sensitivity with a compact scheme.

After having investigated the characteristics of the laser used, and of the various optical elements, the first setup has been designed and built.
The homodyne configuration represented the simplest version, from the points of view of the realization and data acquisition.
The configuration has been studied and the optical configuration was simulated using the software Zemax. Then it has been realized on the optical bench.
Various layouts of the optical components have been explored, as solutions to problems encountered during the experimental project. The best version of the homodyne configuration has been achieved by positioning the crystals orthogonally oriented with respect to each other. This configuration ensured that the polarization of the SH beams generated was orthogonal, and that was a necessary condition to obtain the interferometric signal. The signal has been successfully fitted with the theoretical function, obtaining for the parameters compatible values with the expected ones.
It was found a little discrepancy between the fitted parameters and the expected values, and the main causes identified were the possible presence of absorption effects related to the window, the filters and the polarizer, the imperfect alignment of the window on the rotating support, causing a difference in the experimental optical path, with respect to the one estimated.
For this configuration, the sensitivity has been evaluated, considering the drift which the voltage shows in time, for different time ranges. The sensitivity of the instrument for the evaluation of the line integrated electron density for the time range of 1 s is 3.925 10^{17} m^{-2}.
For a longer time range, of 100 s, the sensitivity obtained is 1.81 10^{18} m^{-2}.

This setup showed very positive results.
An improvement that may be considered is to increase the power of the SH generated by the crystals. Some techniques may be applied, for example positioning the crystals inside cavities, so that the fundamental beam may pass repeatedly inside, generating a higher power SH beam.

During the visit to ENEA laboratories in Frascati, the DI mounted on the experiment PROTO-SPHERA has been studied, and it was possible to work on its re-alignment.
This is a homodyne dispersion interferometer.
Some modifications on the characteristics of the beam focus have been applied to the instrument, to improve the output signal power.
At last, the data collected during the plasma generation in PROTO-SPHERA have been analyzed, obtaining an estimate of the electron density.

A second configuration for the DI for DTT, the heterodyne one, has also been investigated. During the thesis work, the design of this scheme has been conducted.
In this case, the fundamental beam is modulated by an acousto optic modulator (AOM). The working characteristics of this element have been tested, checking if it worked correctly for the fundamental beam. It was positioned at the Bragg angle for the F beam, and the modulated order was successfully observed.
In this same configuration, its effects on the SH beam have also been tested, and it was found that the SH beam power passing through it is heavily cut. This behaviour was observed both with the AOM switched on and off: the conclusions were that probably the material which constitutes the AOM absorbs this wavelength, or the coating presents reflects most of the SH beam.
It was not possible to eliminate the possibility that the AOM works on the SH beam, deviating the beam to the $m = 2$ order, but this effect was considered less probable than the other effects related to the nature of the material.

The next step of the research will be to build the heterodyne DI on the optical bench.
Some problems have surfaced related to the ability of alignment of the dichroic mirrors used to separate the fundamental beam and the SH one. In fact, it was not available any instrument to detect the SH beam except for the photo-diode connected with the oscilloscope, which is not easy to move around the setup. This could be a problem to determine the position of the SH beam deviated by the dichroic mirrors.
The data acquisition system will require the demodulation of the interferometric signal. The photo-diode must be changed, using one with the adequate bandwidth to collect the interferometric signal with the modulation given by the AOM (40 MHz).

In the heterodyne configuration a separation of the paths of the fundamental beam and the SH one needs to be introduced in order to modulate the fundamental one.
Some problems may arise from this: the vibrational components, deriving from the optics which will not be shared by the two beams and will not be eliminated.
To overcome this, two different systems, where one or two prisms are used to deflect the beams, have been studied and designed.
Both of the systems have the aim to deflect the beams so that they both enter the AOM, but with fixed angles so that the shifter only modulates the fundamental beam, but after that element, the beams are superimposed again, and the detection of the interferometric signal is feasible.
A successful design has been completed.
In the future of this work, these configurations will be tested, building customized prisms in order to achieve the conditions required. An issue that may arise is related to the absorption observed for the SH beam when passing through the AOM. This could cause difficulty in observing a good interference signal since one of the two SH beams would be much lower than the other one.

Appendix A

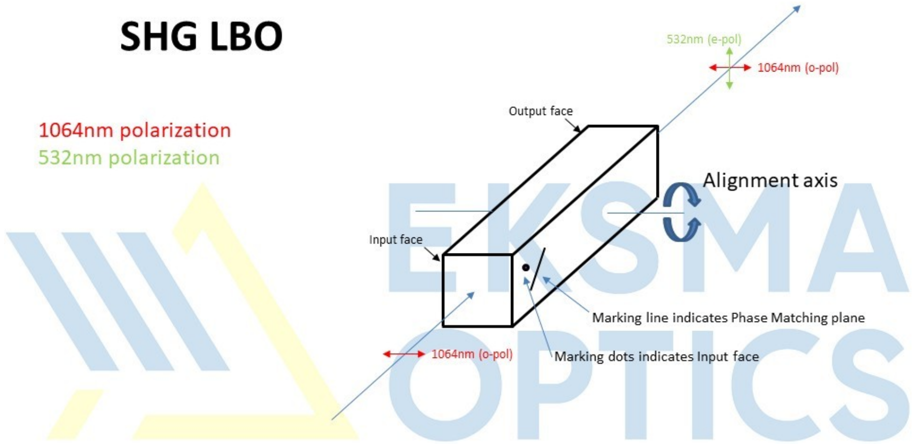

Figure 7.46: Explanatory description of the crystal correct alignment given by the manufacturer. This refers to a different wavelength case: in this work the fundamental beam has wavelength equal to $1.5\mu m$, while the second harmonic beam has wavelength equal to $0.775\mu m$.

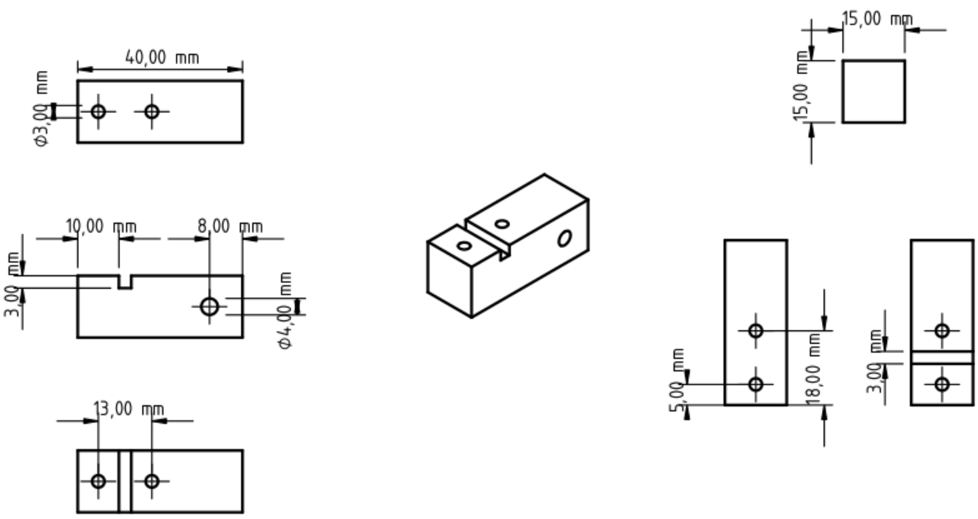

Figure 7.47: Technical design of the first crystal holder made on FreeCad.

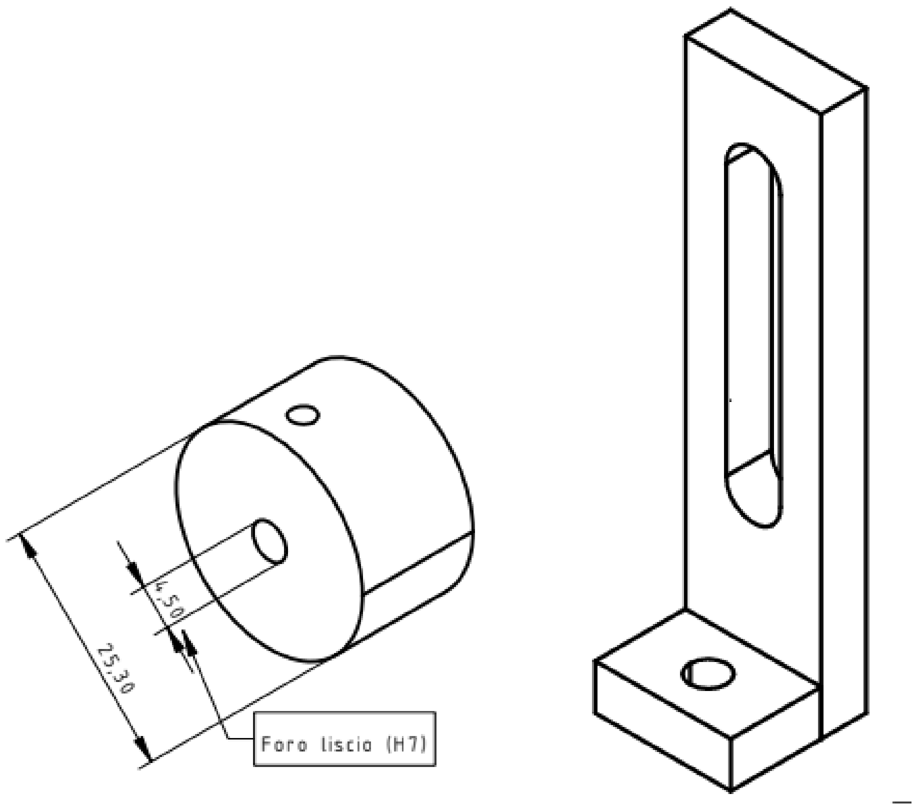

Figure 7.48: Technical design of the second crystal holder and the vertical stage, made on FreeCad.

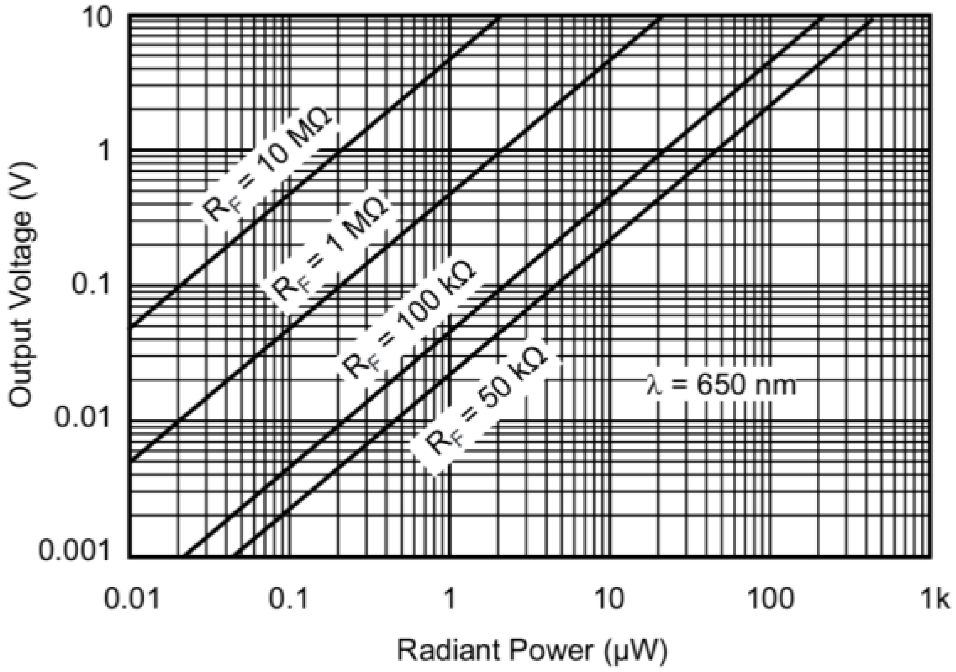

Figure 7.49: Output voltage as a function of the radiant power for the OPT101 Photo-diode, for different values of feedback resistance.

Custom AO Frequency Shifter

- *low power consumption*
- *compact size*

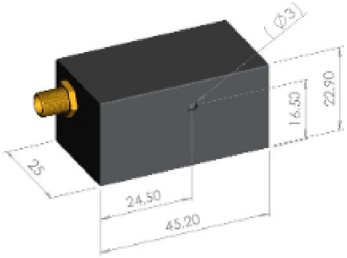

MODEL # AMF-40-20-1550/4mm
Specifications:

Wavelength of Operation	1550 nm
Substrate	AMTIR
Maximum Optical Power	3 W / mm^2
Frequency Shift	40 MHz
Bandwidth (3 dB)	20
Active Aperture	4 mm
Bragg Angle	12 mrad
Separation Angle	25 mrad
Acoustic Velocity (m/sec)	2.5E+3
Optical Transmission	95%
Diffraction Efficiency	~ 70%
Wave Front Distortion	λ/10
Maximum RF Power (Watt)	<1 W
RF Connector	SMA
Extinction Ratio	>1000:1
Input Impedance	50 ohms
V.S.W.R.	2.1:1
Optical Polarization	Any
Case Type	Air Cooled

Brimrose Corporation of America
19 Loveton Circle
Hunt Valley Loveton Center
Baltimore, Maryland 21152-9201 USA

PHONE: 410 - 472 7070
FAX: 410 - 472 7960
EMAIL: office@brimrose.com

www.brimrose.com

V1a97

Figure 7.50: Data sheet of the AO modulator.

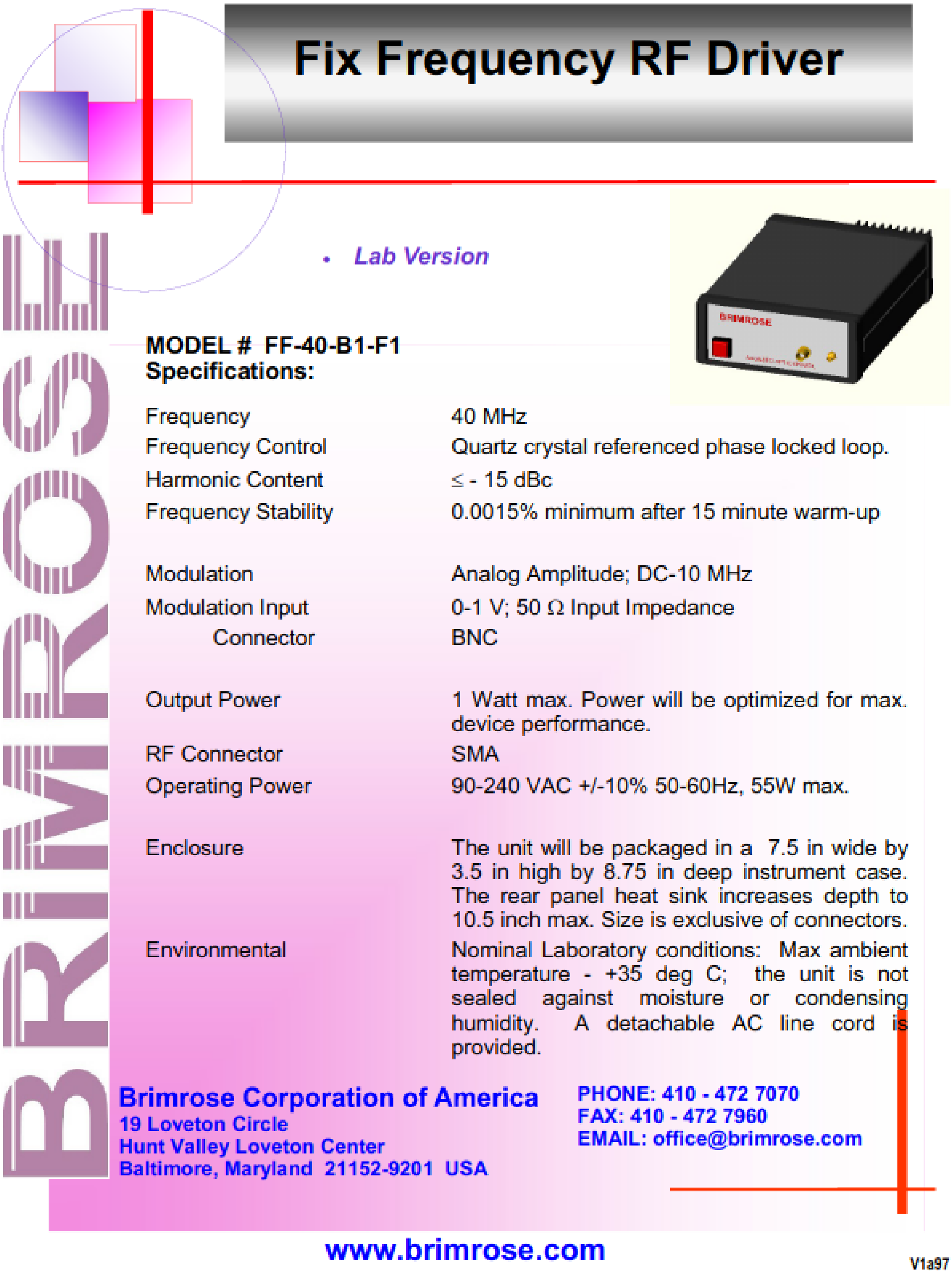

Fix Frequency RF Driver

- *Lab Version*

MODEL # FF-40-B1-F1
Specifications:

Frequency	40 MHz
Frequency Control	Quartz crystal referenced phase locked loop.
Harmonic Content	≤ - 15 dBc
Frequency Stability	0.0015% minimum after 15 minute warm-up
Modulation	Analog Amplitude; DC-10 MHz
Modulation Input	0-1 V; 50 Ω Input Impedance
Connector	BNC
Output Power	1 Watt max. Power will be optimized for max. device performance.
RF Connector	SMA
Operating Power	90-240 VAC +/-10% 50-60Hz, 55W max.
Enclosure	The unit will be packaged in a 7.5 in wide by 3.5 in high by 8.75 in deep instrument case. The rear panel heat sink increases depth to 10.5 inch max. Size is exclusive of connectors.
Environmental	Nominal Laboratory conditions: Max ambient temperature - +35 deg C; the unit is not sealed against moisture or condensing humidity. A detachable AC line cord is provided.

Brimrose Corporation of America
19 Loveton Circle
Hunt Valley Loveton Center
Baltimore, Maryland 21152-9201 USA

PHONE: 410 - 472 7070
FAX: 410 - 472 7960
EMAIL: office@brimrose.com

www.brimrose.com

V1a97

Figure 7.51: Data sheet of the RF driver.

Bibliography

[1] Ian H Hutchinson. "Principles of plasma diagnostics". In: *Plasma Physics and Controlled Fusion* 44.12 (2002), p. 2603.

[2] D Veron. "Interferometry in large plasma machines". In: *Workshop on Diagnostics for Fusion Reactor Conditions*. 1982, pp. 8351–1.

[3] Orazio Svelto and David C Hanna. *Principles of lasers*. Vol. 4. Springer, 1998.

[4] RP-Photonics. *Critical phase-matching*. `https://www.rp-photonics.com/critical_phase_matching.html`. 2021.

[5] DJ Bamford et al. "CO2 laser-based dispersion interferometer utilizing orientation-patterned gallium arsenide for plasma density measurements". In: *Review of scientific instruments* 84.9 (2013), p. 093502.

[6] GD Boyd and DA Kleinman. "Parametric interaction of focused Gaussian light beams". In: *Journal of Applied Physics* 39.8 (1968), pp. 3597–3639.

[7] Frederic A Hopf, Akira Tomita, and G Al-Jumaily. "Second-harmonic interferometers". In: *Optics letters* 5.9 (1980), pp. 386–388.

[8] Kh P Alum, Iu V Kovalchuk, and GV Ostrovskaia. "Nonlinear dispersive interferometer". In: *Pisma v Zhurnal Tekhnischeskoi Fiziki* 7 (1981), pp. 1359–1364.

[9] VP Drachev, Yu I Krasnikov, and PA Bagryansky. "Dispersion interferometer for controlled fusion devices". In: *Review of scientific instruments* 64.4 (1993), pp. 1010–1013.

[10] F Brandi et al. "Electron density measurements of a field-reversed configuration plasma using a novel compact ultrastable second-harmonic interferometer". In: *Review of Scientific Instruments* 80.11 (2009), p. 113501.

[11] PA Bagryansky et al. "Dispersion interferometer based on a CO 2 laser for TEXTOR and burning plasma experiments". In: *Review of scientific instruments* 77.5 (2006), p. 053501.

[12] DTT S.c. a r.l. *DTT-DIVERTOR TOKAMAK TEST facility/Home/The DTT*. `https://www.dtt-project.it/index.php/the-dtt.html`. 2022.

[13] R Albanese, WPDTT2 Team, et al. "DTT: a divertor tokamak test facility for the study of the power exhaust issues in view of DEMO". In: *Nuclear Fusion* 57.1 (2016), p. 016010.

[14] EKSMA Optics. *Enhanced Silver Mirrors*. `https://eksmaoptics.com/optical-components/metallic-mirrors/enhanced-silver-mirrors/`. 2022.

[15] D Veron. "Submillimeter interferometry of high-density plasmas". In: *Infrared and millimeter waves* 2 (1979), pp. 67–135.

[16] Mark Chapman. "Heterodyne and homodyne interferometry". In: *Renishaw, New Mills* (2002).

[17] G Smeets. "Laser interferometer for high sensitivity measurements on transient phase objects". In: *IEEE transactions on Aerospace and Electronic Systems* 2 (1972), pp. 186–190.

[18] T Akiyama et al. "Development of dispersion interferometer for magnetic confinement plasmas and high-pressure plasmas". In: *Journal of Instrumentation* 10.09 (2015), P09022.

[19] Brunello Tirozzi et al. "Theory of the PROTO-SPHERA experiment". In: *Differential Equations on Manifolds and Mathematical Physics* (2021), p. 327.

[20] F Alladio et al. "Design of the PROTO-SPHERA experiment and of its first step (MULTI-PINCH)". In: *Nuclear fusion* 46.8 (2006), S613.

[21] ENEA - C.R. FRASCATI. *Informazioni multimediali/Foto gallery C.R. Frascati.* `https://www.frascati.enea.it/informazioni-multimediali/foto-gallery-c-r-frascati/gli-impianti-protosphera.html`. 2021.

[22] Fernando Brandi and Francesco Giammanco. "Versatile second-harmonic interferometer with high temporal resolution and high sensitivity based on a continuous-wave Nd: YAG laser". In: *Optics letters* 32.16 (2007), pp. 2327–2329.

[23] T Akiyama et al. "Bench testing of a heterodyne CO2 laser dispersion interferometer for high temporal resolution plasma density measurements". In: *Review of Scientific Instruments* 87.12 (2016), p. 123502.

[24] GM Pacheco and JEB Oliveira. "Variable optical attenuator using double acousto-optic modulator". In: *Annals of Optics* 29.1 (2006), pp. 207–216.

[25] Chieu D Tran. "Acousto-Optic Devices". In: *Analytical chemistry* 64.20 (1992), 971A–981A.

[26] S Kakio. "Acousto-optic modulator driven by surface acoustic waves". In: *Acta Phys. Pol. A* 127.1 (2015), pp. 15–19.

[27] O McCormack et al. "On combining the beam path of similar wavelength lasers for dual-laser Thomson scattering". In: *Review of Scientific Instruments* 92.7 (2021), p. 073001.

Acknowledgements

I would like to extend my sincere thanks to my supervisor Prof. Leonardo Giudicotti for all his help and advice and his insightful comments and suggestions.
I would like to express my deepest gratitude to my co-supervisor Dr. Donatella Fiorucci for her assistance at every stage of the research project. She has been of fundamental help for me, not only during this work, but also guiding towards my future steps.
I wish to acknowledge the help provided by the staff at Consorzio RFX.

I would also like to thank my colleagues and friends, Mattia, Andrea, Giulia, Riccardo, Luca and Carlotta, who accompanied me along this path, from the very beginning. Without the sharing of our work this goal would have not been possible to reach.

I would like to extend my sincere thanks to all my dearest friends, Gaia, Anna, Isabella, Beatrice and Francesca. You believed in me when I was only a young girl, and you never stopped. You gave me strength and lightened my days.

I am also very grateful for my family, whom without I would not be the person I am today.
I have to thank you for giving me the opportunity to better myself, while having the best support someone might need.
A special thank to Giacomo, whom with not only I could share my studies, but also my life.
I am so very grateful for everything you do for me and Luce everyday.